

Evolution of Tidal Disruption Event Disks with Magnetically Driven Winds

MAGESHWARAN TAMILAN ¹, KIMITAKE HAYASAKI ¹ AND TAKERU K. SUZUKI ²

¹*Department of Space Science and Astronomy, Chungbuk National University, Cheongju 361-763, Korea*

²*School of Arts and Sciences, The University of Tokyo, 3-8-1, Meguro, Tokyo 153-8902, Japan*

ABSTRACT

We present a time-dependent, one-dimensional, magnetically-driven disk wind model based on magnetohydrodynamic (MHD) equations, in the context of tidal disruption events (TDEs). We assume that the disk is geometrically thin and gas-pressure dominated, and explicitly accounts for magnetic braking and turbulent viscosity through an extended alpha-viscosity prescription. We find a particular wind solution for a set of basic equations that satisfies the necessary and sufficient conditions for vertically unbound MHD flows. The solution shows that the disk evolves with mass loss due to wind and accretion from the initial Gaussian density distribution. We confirm that the mass accretion rate follows the power law of time $t^{-19/16}$ at late times in the absence of wind, which matches the classical solution of Cannizzo et al. (1990). We find that the mass accretion rate is steeper than the $t^{-19/16}$ curve when the wind is present. Mass accretion is also induced by magnetic braking, known as the wind-driven accretion mechanism, which results in a faster decay with time of both the mass accretion and loss rates. In the disk emission, the ultraviolet (UV) luminosity is the highest among the optical, UV, and X-ray luminosities. While the optical and X-ray emission is observationally insignificant without magnetic braking, the X-ray emission is brighter at late times, especially in the presence of magnetic braking. This provides a possible explanation for observed delayed X-ray flares. Our model predicts that late-time bolometric light curves steeper than $t^{-19/16}$ in UV-bright TDEs are potentially compelling indicators of magnetically driven winds.

Keywords: Accretion (14) — Tidal disruption(1696) — Magnetohydrodynamics(1964) — High energy astrophysics(739)

1. INTRODUCTION

A tidal disruption event (TDE) occurs when a star comes close enough to a supermassive black hole (SMBH) to be disrupted by the tidal force of the SMBH. Roughly half of the mass of the disrupted star is bound to the SMBH, while the other half is unbound and escapes from the SMBH. The bound debris falls back to the SMBH at a rate of $-5/3$ power law of time (Rees 1988). However, the mass fallback rate deviates from the $t^{-5/3}$ law at early times due to the stellar density (Lodato et al. 2009), stellar rotation (Golightly et al. 2019) and stellar orbital eccentricity (Hayasaki et al. 2013, 2018; Park & Hayasaki 2020; Cufari et al. 2022; Zhong et al. 2023). Relativistic apsidal precession causes the fallback debris to collide between the head and tail, resulting in the formation of an accretion disk due to its energy dissipation (Hayasaki et al. 2013, 2016; Bonnerot et al. 2016). Once the disk viscosity dominates the evolution of the formed disk at late times, the mass accretion rate is likely to deviate from the mass fallback rate, since the viscous timescale is typically longer than the debris orbital period.

Self-similar solutions for a time-dependent, geometrically thin, and gas pressure-dominated TDE disk with α -viscosity have been developed by Cannizzo et al. (1990). They found that the mass accretion rate is proportional to $t^{-19/16}$ at late times for zero inner stable circular orbit (ISCO) stress at the inner boundary of the disk, which is flatter than

$t^{-5/3}$. Recently, [Mummery & Balbus \(2019\)](#) derived solutions for a general relativistic time-dependent, geometrically thin disk in Kerr spacetime in the context of TDEs. They demonstrated that the late-time bolometric luminosity follows a significantly flatter power law with time than $t^{-19/16}$ for the finite ISCO stress boundary. [Auchetti et al. \(2017\)](#) indicates that the late time light curves of most X-ray TDEs agree with this lower power law index than the classical $t^{-19/16}$ solution, while some other observations suggest a significant deviation from this agreement. For example, the bolometric luminosity of ASASSN-18pg is flatter at late times than the $t^{-5/3}$ law ([Holoien et al. 2020](#)), and the bolometric luminosity of AT2019qiz shows a steep decrease with time, scaling as $t^{-2.54}$ ([Nicholl et al. 2020](#)). Future observations may reveal the diversity of the power law index.

The geometrically thin disk approximation breaks down when the mass accretion rate exceeds the Eddington rate, where the radiation pressure is dominant. A geometrically thin and radiation pressure dominant disk causes the Lightman-Eardley thermal instability ([Lightman & Eardley 1974](#)). Therefore, the advection cooling term in the energy equation is needed to construct a thermally stable slim disk model ([Abramowicz et al. 1988](#)). The strong radiation pressure in the super-Eddington disk causes an outflow from the disk ([Strubbe & Quataert 2009](#); [Gu & Lu 2007](#); [Cao & Gu 2015](#); [Feng et al. 2019](#)). The disk wind obscures the disk emission if the wind is optically thick, reprocessing the X-rays to lower wavelengths. This is thought to make the optical and UV emissions observationally dominant ([Roth et al. 2020](#)). Even if the mass accretion rate is at sub-Eddington, the magnetic field in the disk can trigger the vertical outflow from the disk.

Stars possess magnetic fields that are thought to arise from a dynamo within the stars. Using Zeeman Doppler imaging, [Folsom et al. \(2016\)](#) found that the magnetic fields of 15 young solar-type stars in the mass range $0.7\text{-}1.2 M_{\odot}$ and ages 20-250 Myr have complex large-scale geometries with mean field strengths of 14-140 Gs. Magnetic fields are also ubiquitous in massive stars; $\sim 10^3$ Gs in O stars ([Donati et al. 2002](#); [Petit et al. 2008](#)) and $\sim 3 \times 10^4$ Gs in A and B stars ([Bagnulo et al. 1999](#)). A white dwarf, which is a possible object subject to tidal disruption by intermediate-mass black holes (IMBHs), typically has $\sim 10^9$ Gs ([Schmidt et al. 2003](#)).

The magnetic field strength and configuration within the star are altered by stellar tidal disruption. [Bonnerot et al. \(2017b\)](#) have shown that the magnetic field can promote the circularization process; in particular, both the circularization timescale and the circularization radius decrease with v_A/v_c , where v_A and v_c are the Alfvén velocity and the circular orbital velocity, respectively. This is because the stellar debris loses angular momentum due to magnetic stresses during debris circularization. For a black hole mass of $M = 10^6 M_{\odot}$, the circularization timescale is reduced by an order of magnitude for $v_A/v_c = 0.3$.

[Bonnerot et al. \(2017a\)](#) found that the magnetic field evolution significantly depends on the pericenter of the stellar orbit. The magnetic field strength increases sharply near the pericenter when the star is close to the SMBH for a deep penetrating encounter. This is due to the strong compression of the star prior to the perturbation. They showed that the magnetic field never becomes dynamically critical for complete disruption of a star with an initial stellar magnetic field of 1 Gs. Instead, the full disruption of a star with a magnetic field of 10^6 Gs produces debris streams where the magnetic pressure is comparable to the gas pressure a few tens of hours after the disruption and is crucial for the TDE dynamics.

[Guillochon & McCourt \(2017\)](#) performed numerical magnetohydrodynamic (MHD) simulations of tidally disrupted stars. They showed that as the disrupted debris expands, the component of the magnetic fields perpendicular to the direction of debris stretching decreases, while the magnetic field strength of the component parallel to the stretching increases. The magnetic field configuration in any disk-like structure that forms from the debris is likely to be toroidal.

The magnetic field in the accretion disk impacts the accretion dynamics and results in an astrophysical outflow or jets depending on the strength of the magnetic field. The strong magnetic field in the disk is required to have a jet. For example, the magnetic field required for the jetted TDE Swift J1644+57 is $B \approx 10^8$ Gs ([Tchekhovskoy et al. 2014](#)). Such strongly jetted TDEs could result from the complete disruption of a star with a high magnetic field strength, or after multiple encounters by partial disruption, where the magnetic field of the surviving core is amplified after each passage ([Bonnerot et al. 2017a](#)).

The differential rotation of electrically conducting fluids around a central object causes a magnetorotational instability. (MRI; [Velikhov 1959](#); [Chandrasekhar 1961](#); [Balbus & Hawley 1991, 1998](#)), which induces Maxwell and Reynolds stresses due to the resultant MHD turbulence. The turbulent Maxwell and Reynolds stresses transport angular momentum outwards, driving mass accretion. In addition, vertical outflows are also initiated by the turbulent MHD pressure ([Suzuki & Inutsuka 2009, 2014](#)). The mass loss from such disk winds reduces the accretion rate in the inner disk and the disk luminosity.

Dai et al. (2018) performed a general relativistic radiation magnetohydrodynamics (GRRMHD) simulation of a disk around a black hole of mass $M = 5 \times 10^6 M_\odot$ and spin $j = 0.8$. The initial weak poloidal field (plasma beta of $\sim 20-30$) is amplified by MRI, and a magnetically arrested disk (MAD) is formed up to radius $r \sim 80r_g$, where

$$r_g = \frac{GM}{c^2} \sim 1.5 \times 10^{11} \text{ cm} \left(\frac{M}{10^6 M_\odot} \right) \quad (1)$$

is the gravitational radius, G is the gravitational constant, and c is the speed of light. The accumulated magnetic flux is $\Phi \sim 10^{31} \text{ Gs cm}^{-2}$ and induces a jet due to the high spinning black hole. Along with this, a wide and fast wind is launched from the magnetized disk supported by the radiation pressure, and the outflowing wind reprocesses the radiation from the disk. The recent GRRMHD simulations by Curd & Narayan (2019) of a super-Eddington disk that is formed by the disruption of a solar mass star by $10^6 M_\odot$ black hole mass found that a rapidly spinning black hole and MAD accretion are necessary to produce a jetted TDE, which agrees with the simulation by Dai et al. (2018).

The time evolution of the mass accretion rate and the mass outflow rate is the key to determining the radiation reprocessing dynamics of the disk (Piro & Lu 2020; Roth et al. 2020). The numerical simulations have shown that an outflow with or without a jet arises from the disk (Dai et al. 2018; Curd & Narayan 2019, 2023), but little is known about the long-term evolution of the magnetically driven disk-wind system. Moreover, the classical solution demonstrated that the power-law index is $n = -19/16$ for the late-time variation of the TDE light curves (Cannizzo et al. 1990). However, some observations indicate steeper slopes than $n = -19/16$. Another motivation for our study is to propose a natural theoretical model to explain this steeper decline at late times.

We construct numerical models of one-dimensional gas pressure dominated TDE disks with magnetically driven outflows based on Suzuki et al. (2016) to study their long-term evolution. In section 2, we describe the basic equations of our model and the initial and boundary conditions. In section 3 we present numerical solutions for the basic equations: radial profiles of the disk and wind quantities, as well as the evolution of mass accretion and loss rates, disk mass, and angular momentum. For comparison with observations, we also compute disk spectra and light curves. We discuss our results in section 4. Section 5 is devoted to our conclusions.

2. MODEL

Following Suzuki et al. (2016), we develop a one-dimensional, axisymmetric, time-dependent model with an outflow in cylindrical coordinates $\{r, \phi, z\}$, based on the standard accretion disk model (i.e., a vertically integrated, gas-pressure dominant, geometrically thin viscous accretion disk) with Keplerian rotation $\Omega = \sqrt{GM/r^3}$.

2.1. Basic equations

The pressure of the disk is dominated by the gas pressure, $p_{\text{gas}} = k_B \rho T / \mu m_p$, where ρ is the density, T is the mid-plane temperature of the disk, k_B is the Boltzmann constant, m_p is the proton mass, and μ is the mean molecular weight, assumed to be 0.65. This is the mean molecular weight of the ionized gas for the Sun. We derive the vertical scale height of the disk to be $H = c_s / \Omega$ from the hydrostatic equilibrium for the geometrically thin disk, where the sound speed estimated at the disk midplane is given by $c_s = \sqrt{p_{\text{gas}} / \rho} = \sqrt{k_B T / \mu m_p}$ from the equation of state.

Using the MHD mass and momentum conservation equations given in Balbus & Hawley (1998) with some approximations (see Appendix A.1 for details), we derive the evolution of the disk surface density, $\Sigma = \int_{-H}^H \rho dz \simeq 2H\rho$, as (Suzuki et al. 2016)

$$\frac{\partial \Sigma}{\partial t} - \frac{2}{r} \frac{\partial}{\partial r} \left[\frac{1}{r\Omega} \left\{ \frac{\partial}{\partial r} (\bar{\alpha}_{r\phi} r^2 \Sigma c_s^2) + \bar{\alpha}_{z\phi} r^2 \rho c_s^2 \right\} \right] + \dot{\Sigma}_w = 0 \quad (2)$$

where $\dot{\Sigma}_w \equiv 2\rho v_{z,H}$ is the vertical mass flux, $v_{z,H} \equiv v_z(r, H)$ is the vertical velocity evaluated at the disk scale height H , and $\bar{\alpha}_{r\phi}$ and $\bar{\alpha}_{z\phi}$ are introduced as constant parameters due to the MHD turbulence and disk winds, respectively. According to equations (A11) and (A12), these α parameters are given by

$$\bar{\alpha}_{r\phi} \equiv \frac{1}{c_s^2} \int_{-H}^H \rho \left[v_r \delta v_\phi - \frac{B_r B_\phi}{4\pi\rho} \right] dz \bigg/ \int_{-H}^H \rho dz, \quad (3)$$

$$\begin{aligned} \bar{\alpha}_{z\phi} &\equiv \frac{1}{c_s^2} \left[v_z \delta v_\phi - \frac{B_z B_\phi}{4\pi\rho} \right]_{z=H} \\ &= \frac{4}{(3\tau)^{1/4}} \frac{1}{c_{s,H}^2} \left[v_z \delta v_\phi - \frac{B_z B_\phi}{4\pi\rho} \right]_{z=H} \end{aligned} \quad (4)$$

$$\approx \frac{1}{c_{s,H}^2} \left[v_z \delta v_\phi - \frac{B_z B_\phi}{4\pi\rho} \right]_{z=H}$$

where δv_ϕ is an azimuthal velocity perturbation, (B_r, B_ϕ, B_z) is each component of the B field in cylindrical coordinates, $c_{s,H}$ is the sound velocity evaluated at H , the relation between c_s and $c_{s,H}$ is given by $c_{s,H}^2/c_s^2 = 2/(3\tau)^{1/4} \sim \mathcal{O}(1)$ for $\tau \sim 10 - 100$ with the optical depth τ , and the quantities in the brackets of the equation (4) are evaluated at H . In fact, $\bar{\alpha}_{r\phi}$ and $\bar{\alpha}_{z\phi}$ control how much angular momentum flux is removed radially by accretion and vertically by the winds from the top and bottom of the disk, respectively. The latter parameter corresponds to the magnetic braking; MHD disk winds carry away a significant fraction of the angular momentum from the accretion disk, which triggers mass accretion in the disk. The magnetic braking is quantitatively controlled by the magnetic field strength and the disk-wind flux (Blandford & Payne 1982; Pascucci et al. 2023); in our model setup, the effect of magnetic braking is prescribed in the single parameter $\bar{\alpha}_{z\phi}$.

For the sake of simplicity, we assume that the second term of equation (2) is proportional to the thermal mass flux at the disk mid-plane:

$$\dot{\Sigma}_w = C_w \rho c_s, \quad (5)$$

where C_w is introduced by Suzuki et al. (2010) as a dimensionless proportionality coefficient that is a function of radius and time. The MHD energy equation for an optically thick, Keplerian disk is given by (see Appendix A.2)

$$C_w \rho c_s \left[E_w + \frac{r^2 \Omega^2}{2} \right] + Q_{\text{rad}} = \frac{3}{2} \bar{\alpha}_{r\phi} \Omega \Sigma c_s^2 + \bar{\alpha}_{z\phi} r \Omega \rho c_s^2, \quad (6)$$

where Q_{rad} is the radiative cooling rate:

$$Q_{\text{rad}} = \frac{64\sigma T^4}{3\kappa_{\text{es}}\Sigma} \quad (7)$$

with the Stefan-Boltzmann constant σ and the Thomson scattering opacity $\kappa_{\text{es}} = 0.34 \text{ cm}^{-2} \text{ g}^{-1}$, and E_w is given by equation (A18) as

$$E_w = \frac{1}{2} v^2 + \Phi + \frac{\gamma c_s^2}{\gamma - 1} + \frac{B_\phi^2 + B_r^2}{4\pi\rho} - \frac{B_z}{4\pi\rho v_z} (v_\phi B_\phi + v_r B_r), \quad (8)$$

where Φ is the gravitational potential and γ is the specific heat ratio.

The necessary condition for a disk wind to blow is $E_w \geq 0$, which ensures that the wind material can reach infinity with a positive velocity in the vertical direction. To obtain a particular wind solution, we impose $E_w = 0$ on equation (6) so that we get

$$C_{w,0} \frac{\Sigma r^2 \Omega^3}{4} + Q_{\text{rad}} = \frac{3}{2} \bar{\alpha}_{r\phi} \Omega \Sigma c_s^2 + \frac{1}{2} \bar{\alpha}_{z\phi} r \Sigma \Omega^2 c_s, \quad (9)$$

where $C_{w,0} = C_w(E_w = 0)$ is the normalized mass flux at $E_w = 0$ and we adopt the thin disk approximation:

$$c_s \approx \Omega H. \quad (10)$$

By performing local MHD shearing box simulations for a protoplanetary disk, Suzuki & Inutsuka (2009); Suzuki et al. (2010) elucidated the mass flux of disk winds in a wind onset region where the magnetic energy is roughly equal to the thermal energy, and subsequently they deduced $C_{w,\text{sim}}$ as $10^{-5} \sim 10^{-4}$ (Suzuki et al. 2016). Nevertheless, the estimated value of $C_{w,\text{sim}}$ may be overestimated due to the limitation of the vertical simulation domain. Suzuki et al. (2010) indicated that the vertical mass flux diminishes by a factor of 2 – 3 when simulations are performed with an augmented vertical box size. Consequently, we denote C_w such that

$$C_w = \text{Min}[C_{w,\text{sim}}, C_{w,0}] \quad (11)$$

conservatively.

From equations (2), (7), (9), and (11), we see that there are two basic equations with respect to three variables $(\Sigma, T, C_{w,0})$. Therefore, we introduce an additional equation to make a closure of these equations as

$$Q_{\text{rad}} = \epsilon_{\text{rad}} \left[\frac{3}{2} \bar{\alpha}_{r\phi} \Omega \Sigma c_s^2 + \frac{1}{2} \bar{\alpha}_{z\phi} r \Sigma \Omega^2 c_s \right], \quad (12)$$

where ϵ_{rad} represents a parameter that quantifies the fraction of accretion energy flux converted into radiative cooling flux. Here, the accretion energy is defined as the sum of the viscous heating and the gravitational energy liberated by the inward mass flows, which are driven by the outward transport of angular momentum due to MHD turbulence (characterized by $\bar{\alpha}_{r\phi}$) and the removal of angular momentum via magnetic braking (characterized by $\bar{\alpha}_{\phi z}$). The parameter ϵ_{rad} lies within the range $0 < \epsilon_{\text{rad}} \leq 1$, where $\epsilon_{\text{rad}} = 1$ results in $C_{w,0} = 0$ and $v_z = 0$, corresponding to a standard disk solution without wind (Cannizzo et al. 1990; Frank et al. 2002; Kato et al. 2008). Note that the wind carries away a fraction $(1 - \epsilon_{\text{rad}})$ of the accretion energy.

From equations (2), (7), (9), and (11), the basic equations governing the magnetically-driven disk wind are summarized as follows:

$$\frac{\partial \Sigma}{\partial t} = \frac{2}{r} \frac{\partial}{\partial r} \left[\frac{1}{r\Omega} \frac{\partial}{\partial r} (\bar{\alpha}_{r\phi} r^2 \Sigma c_s^2) \right] + \frac{1}{r} \frac{\partial}{\partial r} (\bar{\alpha}_{z\phi} r \Sigma c_s) - \frac{1}{2} C_{w,0} \Sigma \Omega, \quad (13)$$

$$\frac{1}{4} C_{w,0} \Sigma r^2 \Omega^3 + \frac{64\sigma T^4}{3\kappa_{\text{es}} \Sigma} = \frac{3}{2} \bar{\alpha}_{r\phi} \Omega \Sigma c_s^2 + \frac{1}{2} \bar{\alpha}_{z\phi} r \Omega^2 \Sigma c_s, \quad (14)$$

$$C_{w,0} = (1 - \epsilon_{\text{rad}}) \left[6 \bar{\alpha}_{r\phi} \frac{c_s^2}{r^2 \Omega^2} + 2 \bar{\alpha}_{z\phi} \frac{c_s}{r \Omega} \right], \quad (15)$$

$$c_s = \sqrt{\frac{k_B T}{\mu m_p}} \quad (16)$$

where equation (13) describes the temporal evolution of the surface density, equation (14) gives the radial profile of the mid-plane temperature of the disk, and equation (15) determines $C_{w,0}$, for which we employ equations (9) and (12) in its derivation. Equation (16), which originates from the ideal gas equation of state, gives the relation between c_s and T . We solve equations (13)-(16) simultaneously to get the time evolution of the disk with wind.

2.2. Initial and boundary conditions with model parameters

In our models, we postulate an SMBH mass of $M = 10^6 M_\odot$ with the solar-type star. The tidal disruption radius is then given by

$$\begin{aligned} r_t &\simeq \left(\frac{M}{M_\star} \right)^{1/3} R_\star \\ &\sim 7.0 \times 10^{12} \text{ cm} \left(\frac{M}{10^6 M_\odot} \right)^{1/3} \left(\frac{M_\star}{M_\odot} \right)^{-1/3} \left(\frac{R_\star}{R_\odot} \right) \end{aligned}$$

(Hills 1975), where M_\star and R_\star are the stellar mass and radius, respectively.

The conservation of the angular momentum of stellar debris provides the circularization radius of stellar debris to be (Strubbe & Quataert 2009; Hayasaki et al. 2016)

$$\begin{aligned} r_c &= \frac{(1 + e_\star) r_t}{\beta} = 2r_t \\ &\sim 1.4 \times 10^{13} \text{ cm} \left(\frac{M}{10^6 M_\odot} \right)^{1/3} \left(\frac{M_\star}{M_\odot} \right)^{-1/3} \left(\frac{R_\star}{R_\odot} \right) \end{aligned}$$

where e_\star and β are, respectively, the stellar orbital eccentricity and the penetration factor, which is the ratio of the tidal disruption radius to the pericenter radius. We adopt $e_\star = 1.0$ and $\beta = 1.0$ as standard TDE cases. Note that the circularization radius is also expressed as $r_c \simeq 94 r_g (M/10^6 M_\odot)^{-2/3} (M_\star/M_\odot)^{-1/3} (R_\star/R_\odot)$ in units of the gravitational radius (see equation 1). Magnetic stress may reduce the circularization radius (Bonnerot et al. 2017b) during the circularization process, but we do not take it into account because doing so would require detailed knowledge of the magnetic field strength and configuration in the debris. Additionally, we neglect any mass and angular momentum loss due to debris stream-stream collisions for simplicity, assuming that a ring-structured accretion disk is formed with half of the disrupted debris bound to the SMBH, $M_\star/2$. The surface density of the disk initially has a Gaussian distribution with a peak at r_c .

$$\Sigma = \Sigma_0 \exp \left[-\frac{(r - r_c)^2}{\varpi^2} \right] \quad (17)$$

Table 1. Four models are employed to evaluate the evolution of magnetically-driven accretion disk-winds. Model I represents a geometrically thin disk with no disk wind, while Models II-IV depict disks with outflows, each characterized by different parameters.

Model	ϵ_{rad}	$\bar{\alpha}_{r\phi}$ Turbulent viscosity	$\bar{\alpha}_{z\phi}$ Magnetic braking	Wind
I	1.0	0.1	0	Off
II	0.1	0.1	0	On
III	0.5	0.1	0	On
IV	0.5	0.1	0.001	On

(Cannizzo et al. 1990), where ϖ is the width of the Gaussian disk, which is taken to be $3r_g$ ¹. In addition, Σ_0 shows the surface density of the initial disk at $r = r_c$:

$$\Sigma_0 = M_i / \left(2\pi \int_{r_{\text{in}}}^{r_{\text{out}}} r \exp \left[-\frac{(r - r_c)^2}{\varpi^2} \right] dr \right), \quad (18)$$

where M_i is the initial disk mass, which is assumed to be $0.5M_\odot$ as a fiducial value², $r_{\text{in}} = 6r_g$ is the inner boundary of the calculation domain, corresponding to the inner stable circular orbit (ISCO) radius for a non-spinning black hole, and $r_{\text{out}} = 10^4 r_g$ is the outer radius of the disk, corresponding to the outer boundary of the calculation domain. As an additional boundary condition, we set the surface density at the inner and outer radii of the disk to zero (Cannizzo et al. 1990). The matter at the inner radius is accreted onto the black hole, while the matter at the outer radius is expelled from the system. Since $r_{\text{out}} \gg r_{\text{in}}$, the viscous timescale for the matter to reach the outer radius is much longer than the evolution time of our calculations, ensuring that the outer boundary has no influence on the structure and evolution of the system. Furthermore, zero surface density at r_{in} implies vanishing viscous stress at the inner radius. These two conditions ensure that the total angular momentum of the disk is conserved in the absence of disk wind.

Table 1 shows the four models we calculated. Model I represents the standard disk with no wind, while the other models simulate the evolution of magnetically-driven accretion disk winds with different sets of parameters for $(\epsilon_{\text{rad}}, \bar{\alpha}_{z\phi})$. For all models, we adopt $\bar{\alpha}_{r\phi} = 0.1$ and $C_{\text{w,sim}} = 2 \times 10^{-5}$ (Suzuki et al. 2016). Figure 1 depicts the initial surface density distribution given by equation (17) and the corresponding mid-plane temperature for all models. According to equation (12), a decrease in ϵ_{rad} reduces the radiative flux, resulting in a lower temperature. In contrast, an increase in $\bar{\alpha}_{z\phi}$ leads to an increase in the radiative flux, thereby raising the disk temperature.

The α viscosity prescription $\nu = \alpha c_s H$ and the thin disk approximation (see equation 10) provide the time normalization at r_c as

$$\begin{aligned} \tau_0 &\equiv \frac{r_c^2}{\nu} \approx \frac{1}{\bar{\alpha}_{r\phi} \Omega} \left(\frac{H}{r_c} \right)^{-2} \\ &\sim 14.3 \text{ yr} \left(\frac{\bar{\alpha}_{r\phi}}{0.1} \right)^{-1} \left(\frac{H/r_c}{0.01} \right)^{-2} \end{aligned} \quad (19)$$

throughout the paper, where we adopt the disk aspect ratio as a constant, i.e., $H/r_c = 0.01$, for the purpose of comparing the results among the different models.

¹ There is no remarkable difference between $\bar{\omega} = 3r_g$ and $\bar{\omega} = 0.1r_c \sim 9.4r_g$ once the disk evolves after $t/\tau_0 = 0.01$, although their initial distributions are distinguishable

² The effect of M_i on the results is discussed in section 3.5

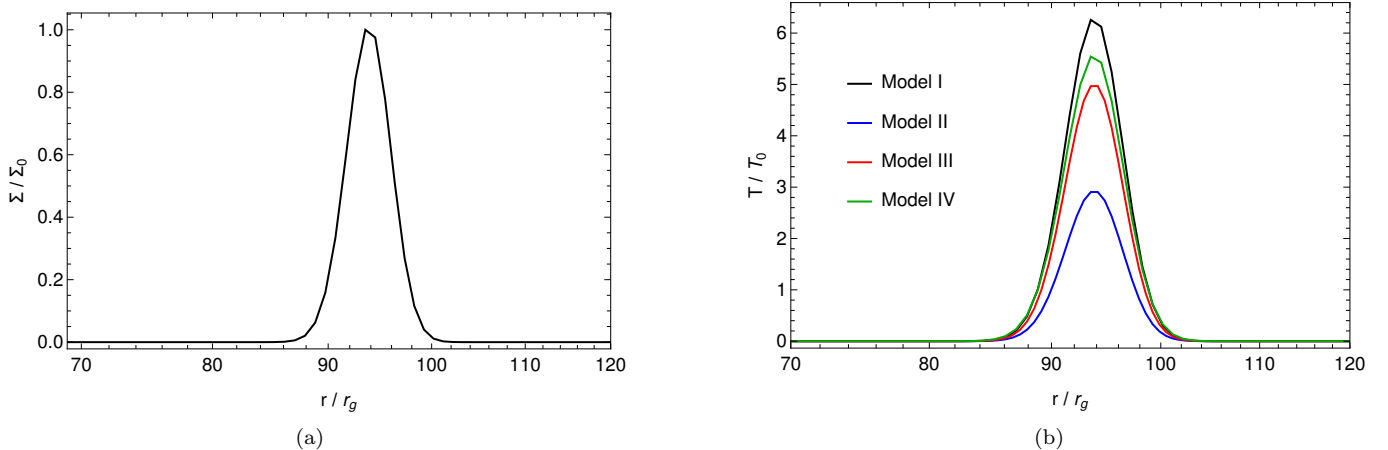


Figure 1. Initial radial distribution of the surface density (see equation 17) and corresponding radial profiles of the disk mid-plane temperature for the four models. These profiles are displayed in panels (a) and (b), respectively. In panel (a), the surface density is normalized to $\Sigma_0 = 1.45 \times 10^7 \text{ g cm}^{-2}$, and in panel (b), the disk temperature is normalized to $T_0 = 1.0 \times 10^6 \text{ K}$. Note that the radial surface density profile is identical for all models.

3. RESULTS

In this section, we show the solutions for equations (13)-(16) with the initial and boundary conditions described in Section 2.2.

3.1. Evolution of radial profiles of disk and wind quantities

Figure 2 shows the radial profiles of the surface density, disk mid-plane temperature, disk aspect ratio, and wind mass flux for Models I through III at three early time epochs. Each panel includes an inset displaying the radial profile of each quantity at a later time epoch, $t/\tau_0 = 30$. These models differ in the values of ϵ_{rad} , while $\bar{\alpha}_{z\phi}$ is kept constant at zero. The initial Gaussian disk spreads with time both radially inward and outward due to disk viscosity. Mass accretion increases the surface density and temperature near the inner radius at later times. The disk aspect ratio remains well below unity, indicating that the disk is geometrically thin at all time epochs.

Panels (a) to (c) show that disk temperature and H/r increase in the order of Models I, III, and II, indicating that these quantities are higher for larger values of ϵ_{rad} . Since the viscous timescale is estimated as $r^2/\nu \propto \bar{\alpha}_{z\phi}^{-1} T^{-1}$, it correspondingly decreases in the same order. This suggests that the disk evolves more rapidly as ϵ_{rad} increases, because a larger fraction of the liberated energy is transferred to the thermal component, resulting in a higher temperature.

Now, focusing on the radial profile of the surface density for each model, as shown in panel (a), equation (15) indicates that the energy available for mass loss increases as ϵ_{rad} decreases, leading to a higher vertical mass flux. This is consistent with the result that the vertical mass flux of Model II is larger than that of Model III at $t/\tau_0 = 0.01$, as shown in panel (d). If mass loss proceeds efficiently, the surface density should decrease more rapidly. However, the surface density of Model II is higher than that of Model III, which appears to contradict this expectation.

How can we interpret the seemingly contradictory results at $t/\tau_0 = 0.01$? These results can be understood by considering two factors. First, although $(1 - \epsilon_{\text{rad}})$ determines the efficiency of the mass-loss rate, the actual mass-loss rate also depends on the surface density. This implies that a higher efficiency does not necessarily lead to a higher mass-loss rate. Second, there is a competition between viscous accretion and wind mass loss in the evolution of the disk's surface density. The viscous effect dominates the early evolution of Models II and III. Specifically, since the viscous timescale is shorter in Model III than in Model II, the surface density of Model III evolves more rapidly, resulting in the opposite trend at early times compared to later times.

Figure 3 presents the same format as Figure 2, but for the scenario with a non-zero value of $\bar{\alpha}_{z\phi}$, referred to as Model IV. For comparative purposes, the characteristics of Model III are also shown in the same figure. According to panels (a) and (d) of the figure at early times, there is little difference between Models III and IV in terms of surface density, while the vertical mass flux shows a significant difference. This indicates that $\bar{\alpha}_{z\phi}$ has minimal impact on surface density evolution but significantly affects the vertical mass flux, which will be discussed in more detail later in

this subsection. From panels (b) and (c), we observe that $\bar{\alpha}_{z\phi}$ has a mild influence on the disk mid-plane temperature and the disk aspect ratio evolution. In contrast to the behavior at $t/\tau_0 = 1.0$, the surface density, disk mid-plane temperature, H/r , and $\dot{\Sigma}_w$ of Model IV are overall lower than those of Model III at $t/\tau_0 = 30$. This is due to the significantly rapid decay of the mass accretion and loss rates caused by magnetic braking from early to late times (see also Figures 7 and 8).

The mass accretion rate is obtained using equation (A13) as

$$\dot{M} = -2\pi r \Sigma v_r = \frac{4\pi}{r\Omega} \left[\frac{\partial}{\partial r} (\bar{\alpha}_{r\phi} r^2 \Sigma c_s^2) + \bar{\alpha}_{z\phi} r^2 \rho c_s^2 \right]. \quad (20)$$

The mass accretion rate is positive for $v_r < 0$, indicating a radial inflow of the gas to the black hole, whereas the mass accretion rate is negative for $v_r > 0$, indicating a radial outflow.

As a result of wind blowing vertically, mass is lost at a rate of

$$\dot{M}_w = \int \dot{\Sigma}_w 2\pi r dr = \pi \sqrt{GM} \int_r^{r_{\text{out}}} \frac{C_w \Sigma}{\sqrt{r}} dr, \quad (21)$$

where we used equation (5) with equation (10) for the derivation.

Figure 4 shows the radial profiles of the mass accretion rate (\dot{M}) and the mass loss rate (\dot{M}_w) at different time epochs for Models I through III. Both rates are normalized by the Eddington accretion rate:

$$\dot{M}_{\text{Edd}} = \frac{L_{\text{Edd}}}{\eta c^2} \sim 2.6 \times 10^{-2} M_{\odot}/\text{yr} \left(\frac{\eta}{0.1} \right)^{-1} \left(\frac{M}{10^6 M_{\odot}} \right), \quad (22)$$

where

$$L_{\text{Edd}} = \frac{4\pi GMc}{\kappa_{\text{es}}} \approx 1.5 \times 10^{44} \text{ erg s}^{-1} \left(\frac{M}{10^6 M_{\odot}} \right) \quad (23)$$

is the Eddington luminosity, and η is the radiative efficiency, with a fiducial value of 0.1 for the Eddington accretion rate. A positive value of \dot{M} indicates an inward accretion flow, while a negative value of \dot{M} denotes an outward decretion flow. The mass loss rate represents the outflowing wind from the disk's upper and lower surfaces and is always positive.

Figure 5 depicts the radial profiles of the mass accretion and loss rates for Models III and IV at $t/\tau_0 = 0.01$, $t/\tau_0 = 0.1$, $t/\tau_0 = 1.0$, and $t/\tau_0 = 30$, respectively. The figure shows that, at early times, both the mass accretion and loss rates of Model IV are higher across the disk's entire region up to $100 r_g$ compared to those of Model III. This is due to the magnetocentrifugal effect resulting from the non-zero value of $\bar{\alpha}_{z\phi}$ (Blandford & Payne 1982), which directly removes angular momentum from the disk and facilitates mass accretion onto the central object. This wind-driven accretion leads to additional liberation of gravitational energy, increasing the kinetic energy of the disk winds. Consequently, the mass loss rate also increases due to the presence of $\bar{\alpha}_{z\phi}$. The enhanced mass accretion and loss rates of Model IV compared to Model III at early times rapidly deplete the disk's mass in Model IV, leading to a lower surface density at late times (see the inset of Figure 3a for $t/\tau_0 = 30$). Consequently, this depletion causes the mass accretion and loss rates of Model IV to become lower than those of Model III at $t/\tau_0 = 30$.

Let us consider the radial distribution of $C_{w,0}$, which is approximated by using equation (15) along with equation (10) as follows:

$$C_{w,0} \approx 2(1 - \epsilon_{\text{rad}}) \left[3\bar{\alpha}_{r\phi} \left(\frac{H}{r} \right)^2 + \bar{\alpha}_{z\phi} \left(\frac{H}{r} \right) \right] \quad (24)$$

This expression allows us to analytically obtain $C_{w,0} < C_{w,\text{sim}}$ when $\bar{\alpha}_{r\phi} = 0.1$, $\bar{\alpha}_{z\phi} = 0$ or $\bar{\alpha}_{z\phi} = 1.0 \times 10^{-3}$, and $H/r \lesssim 5 \times 10^{-3}$. Figure 6 displays the radial dependence of $C_{w,0}$. As shown in the figure, for all models and time epochs, $C_{w,0}$ is slightly smaller than the fiducial value, which is consistent with the analytical estimation. Additionally, $C_{w,0}$ decreases with time over the entire disk. Assuming $\bar{\alpha}_{r\phi} = 0$, from equations 11 and 24, we find that the vertical mass flux is simply proportional to $\bar{\alpha}_{z\phi}(H/r)$ through $C_{w,0}$. This is the primary reason why the vertical mass flux is higher at early times than in the case of $\bar{\alpha}_{z\phi} = 0$, as shown in Figure 3.

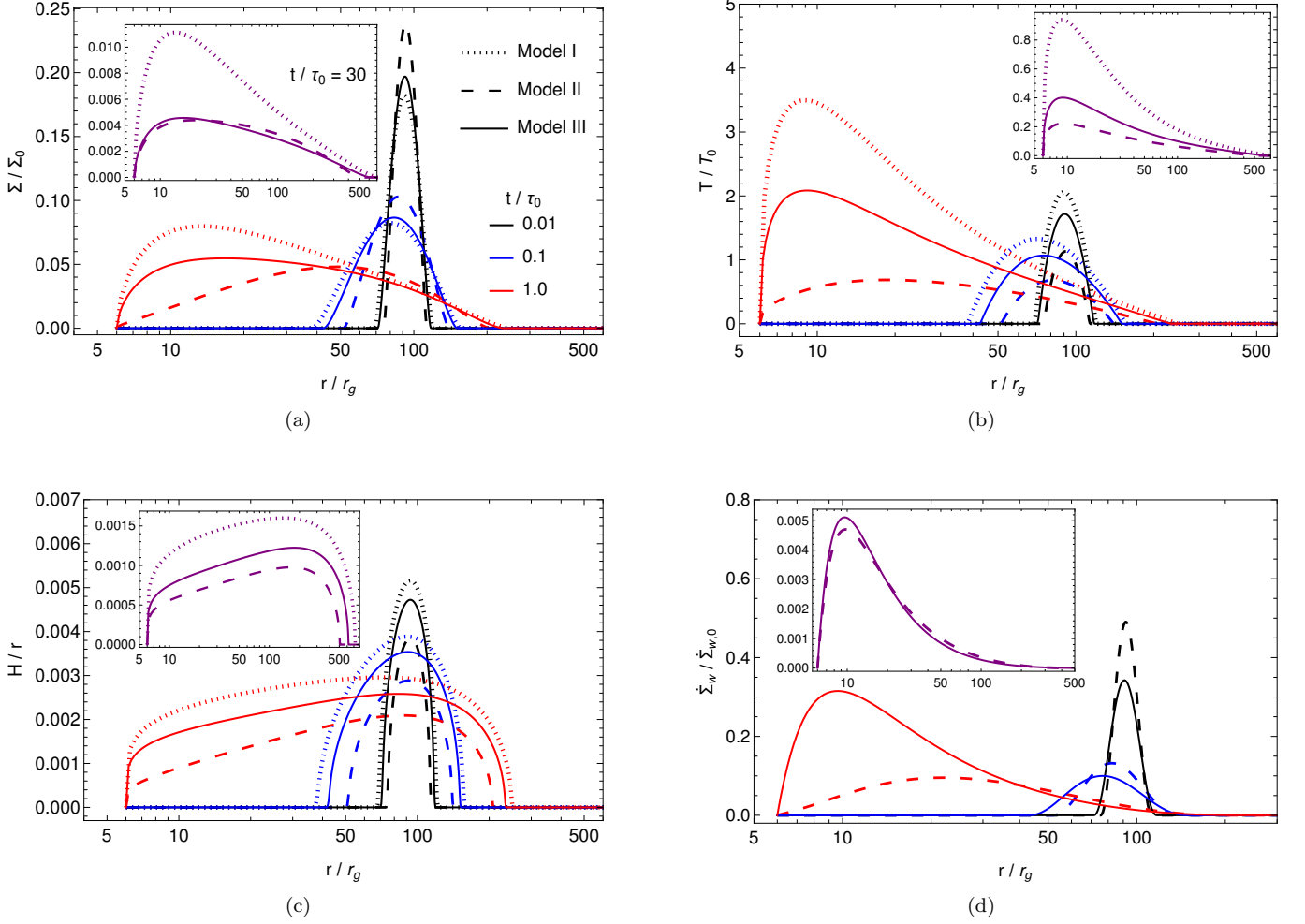


Figure 2. Radial profiles of the surface density, disk mid-plane temperature, disk aspect ratio, and vertical mass flux for Models I through III. For all three models, $\bar{\alpha}_{z\phi} = 0$, with different values of ϵ_{rad} : 1.0 (Model I), 0.1 (Model II), and 0.5 (Model III). Panel (a) shows the profiles with $\tau_0 = 14.3$ yr and $\Sigma_0 = 1.45 \times 10^7 \text{ g cm}^{-2}$, panel (b) shows the profiles with $T_0 = 1.0 \times 10^6 \text{ K}$, panel (c) shows the disk aspect ratio, and panel (d) shows the profiles with $\dot{\Sigma}_{w,0} = 6.4 \times 10^{-3} \text{ gs}^{-1} \text{ cm}^{-2}$. The inset in each panel displays the corresponding physical quantity at a very late time, $t/\tau_0 = 30$.

3.2. Evolution of mass accretion and mass-loss rates

Panel (a) of Figure 7 shows the time evolution of the mass accretion rate estimated at r_{in} for Models I through IV. The peak mass accretion rate increases with ϵ_{rad} or $\bar{\alpha}_{z\phi}$. It is important to note that $\bar{\alpha}_{z\phi}$ governs magnetic braking in the disk, while ϵ_{rad} controls the fraction of the total heating flux in the disk that is converted into radiative cooling flux. Higher values of these two parameters result in more efficient angular momentum loss, thereby increasing the mass accretion rate. When $\bar{\alpha}_{z\phi} = 0$, the mass accretion rate overall increases as ϵ_{rad} approaches 1.

The presence of a wind ($0 < \epsilon_{\text{rad}} < 1$) causes the slopes of the \dot{M} decay curves to steepen with time, as evident from the panel. Assuming $\dot{M} \propto t^n$, the slope is expressed by the power-law index n of the mass accretion rate curve:

$$n = \frac{d \ln(\dot{M})}{d \ln t} \quad (25)$$

Panel (b) of Figure 7 shows the time dependence of n for $0 \leq t/\tau_0 \leq 30$. The small inset illustrates the variation of n at very early times. In all models, n initially rises sharply and then rapidly decreases, demonstrating the quick transition from an increasing to a decreasing \dot{M} , as shown in panel (a). In Models I to III, n asymptotes to specific values at late times. In the absence of wind ($\epsilon_{\text{rad}} = 1$), n asymptotes to $-19/16$ at late times, which corresponds to

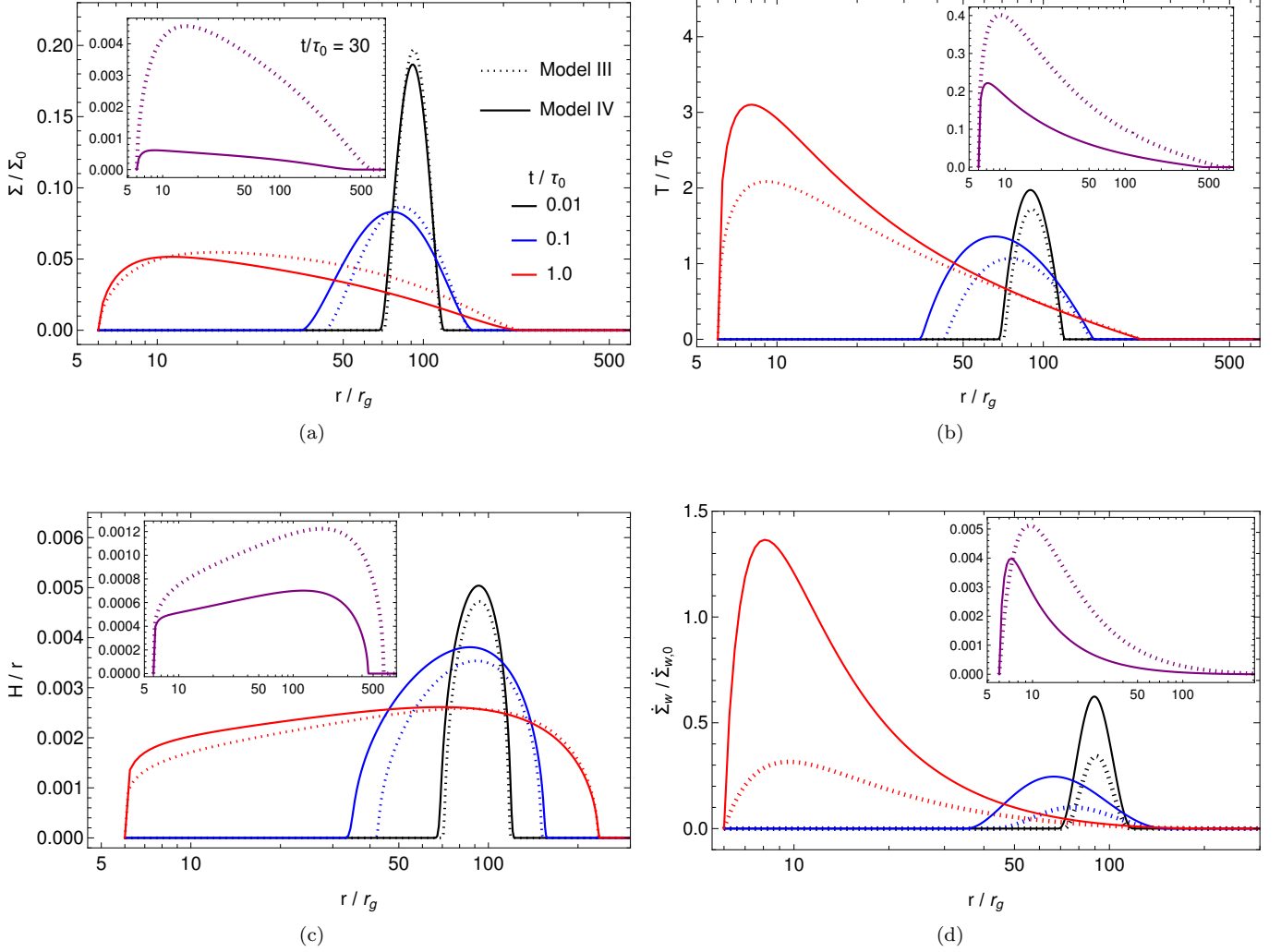


Figure 3. The same format as Figure 2 but for Models III and IV.

the solution by Cannizzo et al. (1990). When wind is present, the power-law index asymptotes to -1.62 in Model II, while it asymptotes to -1.52 in Model III. This suggests that the slope becomes slightly steeper as ϵ_{rad} decreases. Comparing Model III and IV, the slope is significantly steeper without saturation at the non-zero value of $\bar{\alpha}_{z\phi}$.

Panel (a) of Figure 8 shows the mass loss rate for Models II through IV at different time epochs. From the figure, it can be observed that the mass loss rates of Models II and III slowly decay at early times, followed by a rapid decrease. In contrast, the mass loss rate of Model IV exhibits a small peak around $t/\tau_0 \approx 0.4$, followed by a rapid decay after the peak. Magnetic braking, characterized by $\bar{\alpha}_{z\phi}$, significantly affects the magnitude and slope of the mass loss rate, while the effect of ϵ_{rad} is less pronounced.

The mass loss rates of Models II and III follow a power-law evolution at late times. The power law index of time of the mass loss rate, similar to equation (25), is given by

$$n_w = \frac{d \ln(\dot{M}_w)}{d \ln t} \quad (26)$$

Panel (b) of Figure 8 shows the time dependence of n_w for $0 \leq t/\tau_0 \leq 30$. The small inset shows the time variation of n_w at very early times. In Models II and III, n_w asymptotes to lower values than n , while n_w in Model IV shows no saturation within our calculation time.

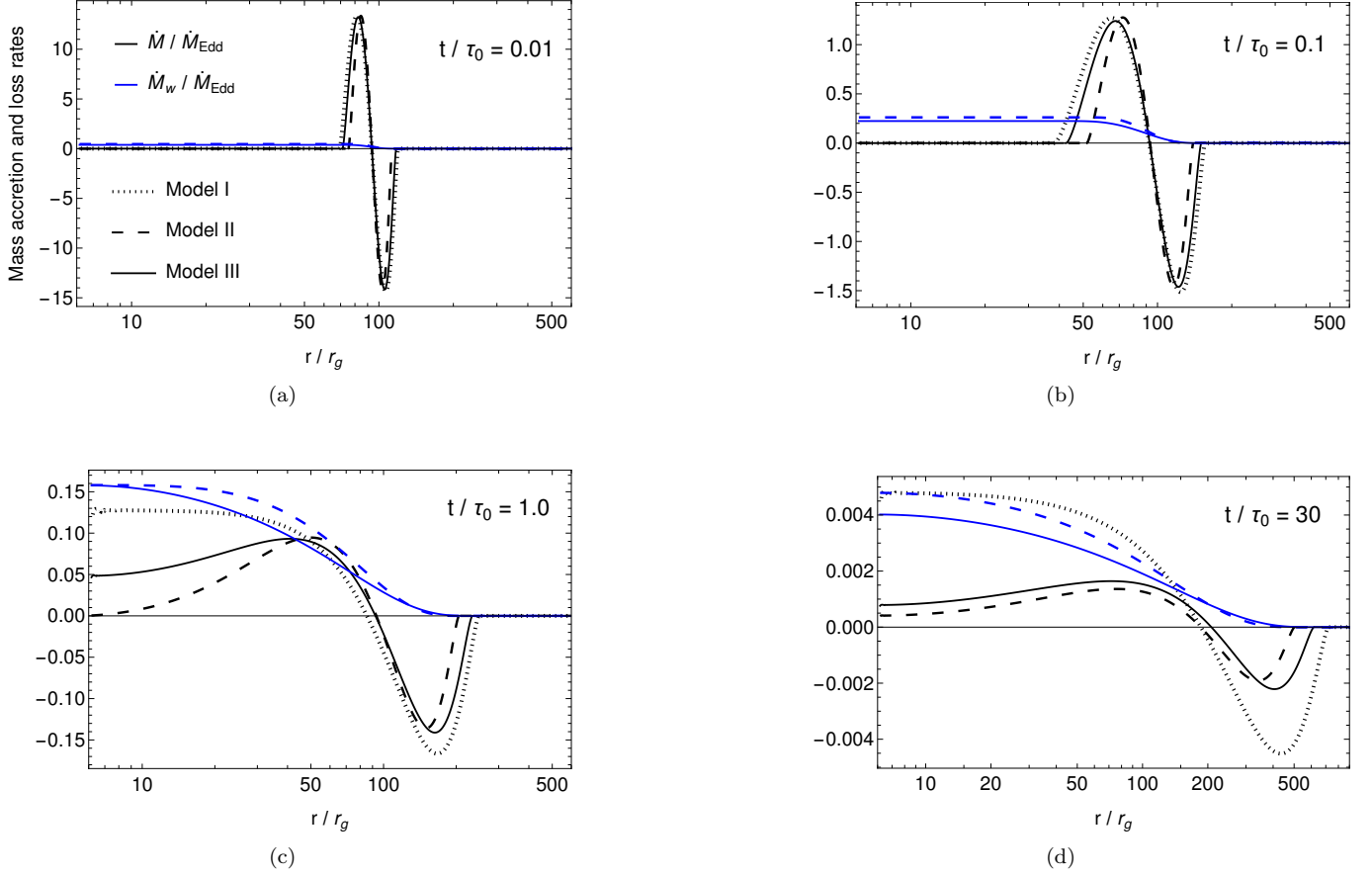


Figure 4. Radial dependence of the mass accretion rate (solid lines) and the mass wind rate (dashed lines) for Models I through III, as obtained using equations (20) and (21), respectively. Panels (a) to (d) show the results at $t/\tau_0 = 0.01$, $t/\tau_0 = 0.1$, $t/\tau_0 = 1.0$, and $t/\tau_0 = 30$, respectively. The mass accretion rate is represented by black solid lines and the mass wind rate by blue dashed lines, with both rates normalized by the Eddington accretion rate. Different line styles indicate different models. Note that there is no blue line for Model I, as there is no wind present for $\epsilon_{\text{rad}} = 1.0$.

The disk mass and angular momentum are given by

$$M_{\text{d}} = 2\pi \int_{r_{\text{in}}}^{r_{\text{out}}} r \Sigma \, dr,$$

$$J_{\text{d}} = 2\pi \int_{r_{\text{in}}}^{r_{\text{out}}} r^3 \Omega \Sigma \, dr,$$

respectively.

Panel (a) of Figure 9 shows the time evolution of the total disk mass. The initial disk mass corresponds to half of the stellar mass, and this value is used for mass normalization. As the disk evolves, its mass decreases with time. In Model I, the decrease is attributed to mass loss via accretion, whereas in Models II to IV, the disk mass decreases more rapidly due to both accretion and wind. In particular, a comparison between Models II and III indicates that M_{d} shows only a weak dependence on ϵ_{rad} . Furthermore, comparing Models III and IV demonstrates that wind-driven accretion with a non-zero value of $\bar{\alpha}_{z\phi}$ significantly reduces the disk mass.

Panel (b) of Figure 9 shows the time evolution of the total angular momentum of the disk. In the absence of the wind ($\epsilon_{\text{rad}} = 1$), the total angular momentum of the disk is conserved due to the zero viscous torque at the inner boundary of the disk, even though mass is lost, as indicated in panel (a). This confirms that our numerical calculations are accurate. When the wind is present, it carries away angular momentum from the disk, resulting in a decrease in

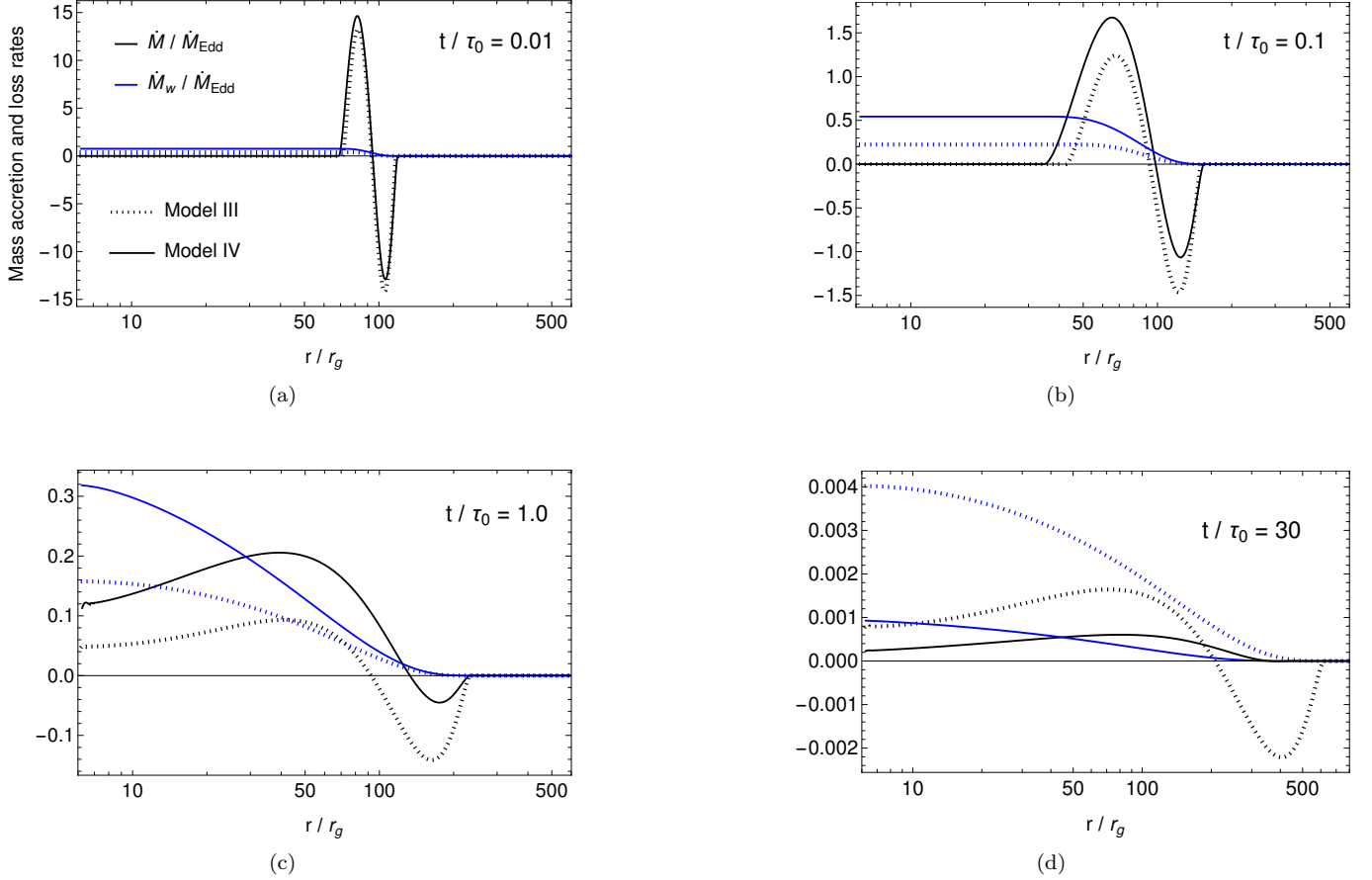


Figure 5. The same format as Figure 4 but for Models III and IV.

J_d for $0 < \epsilon_{\text{rad}} < 1$. The dependence of J_d on ϵ_{rad} and $\bar{\alpha}_{z\phi}$ exhibits the same trend as the M_d evolution for Models II-IV.

3.3. Disk spectra and light curves

In this subsection, we compute the disk spectra for all models and describe the spectral properties of the disk in the combined disk and wind system. Since the effective temperature is given by $T_{\text{eff}} = (Q_{\text{rad}}/2\sigma)^{1/4}$ and equation (7) relates T_{eff} to the disk mid-plane temperature T , T_{eff} can be determined numerically. Because the disk is highly optically thick, the observed flux is given using Planck's blackbody distribution by

$$F_{\nu, \text{obs}} = 2\pi \frac{\cos \theta_{\text{los}}}{D_L^2} \int_{r_{\text{in}}}^{r_{\text{out}}} B_\nu(T_{\text{eff}}, \nu) r dr, \quad (27)$$

where θ_{los} is the angle between the observer's line of sight and the disk normal vector, D_L is the luminosity distance from the source to the observer. The disk luminosity of a certain frequency range of $\nu_l \leq \nu \leq \nu_u$ is expressed by

$$L = \int_{\nu_l}^{\nu_u} L_\nu d\nu, \quad (28)$$

where L goes to the bolometric luminosity, L_b , at $\nu_l \rightarrow 0$ and $\nu_u \rightarrow \infty$, and L_ν is the spectral luminosity:

$$L_\nu = 4\pi D_L^2 F_{\nu, \text{obs}} = 8\pi^2 \cos \theta_{\text{los}} \int_{r_{\text{in}}}^{r_{\text{out}}} B_\nu(T_{\text{eff}}, \nu) r dr, \quad (29)$$

where the right-hand side is derived using equation (27). In our calculations, we adopt $\theta_{\text{los}} = 0^\circ$, corresponding to an observer viewing the entire disk from a pole-on perspective.

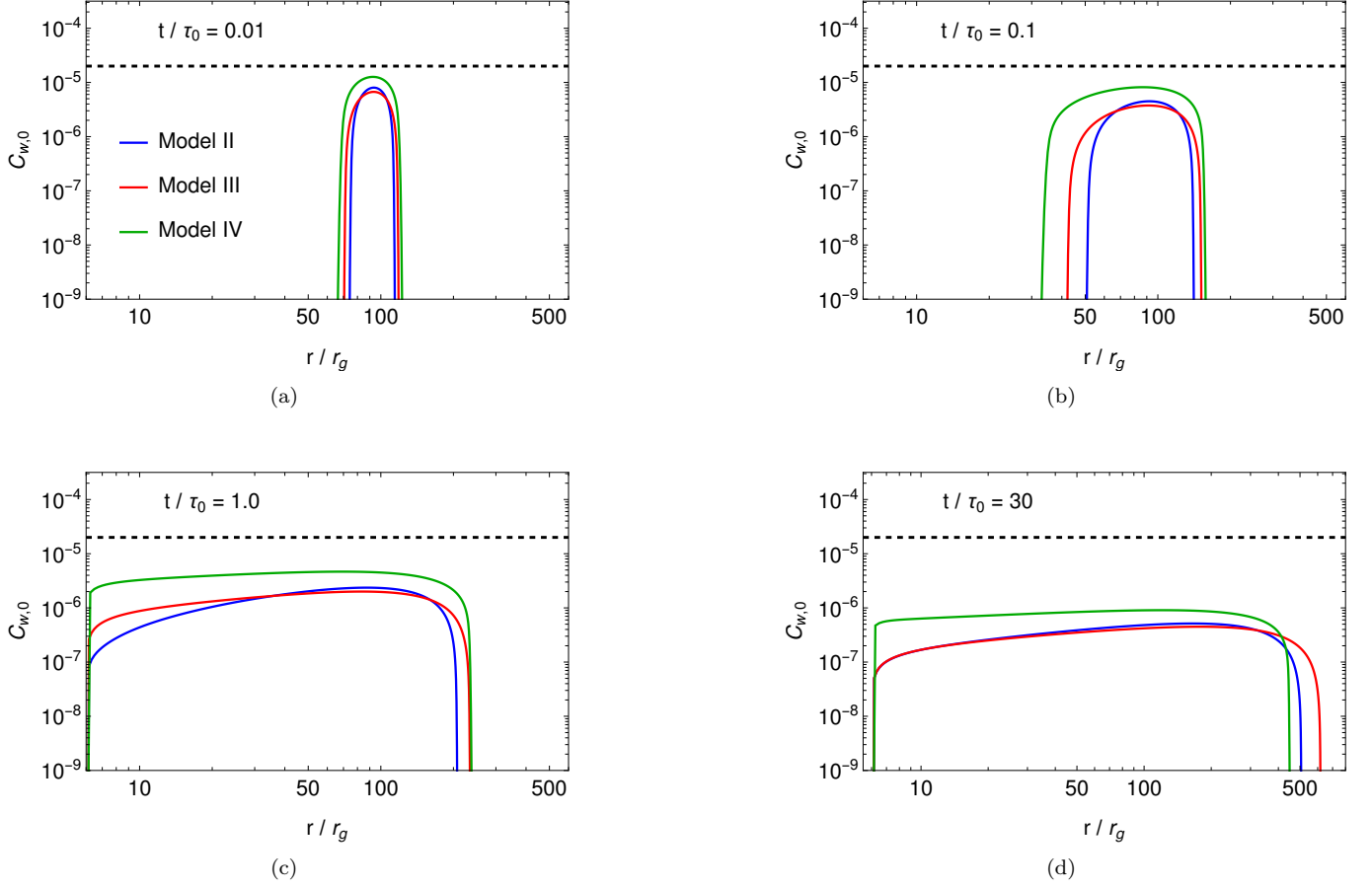


Figure 6. Radial profiles of $C_{w,0}$, obtained using equation (15), for Models II through IV at different time epochs. Panels (a) to (d) show profiles at $t/\tau_0 = 0.01$, $t/\tau_0 = 0.1$, $t/\tau_0 = 1.0$, and $t/\tau_0 = 30$, respectively, displayed chronologically. In each panel, different colors represent different models. The black dashed line indicates the $C_{w,\text{sim}} = 2 \times 10^{-5}$ line, obtained from simulations (Suzuki et al. 2016), which serves as the fiducial value.

Figure 10 illustrates the disk spectra of Models I to IV at different times. As can be seen in the figure, the disk spectra exhibit peaks ranging from the far ultraviolet (UV) to the mid-UV at early times, with the peaks gradually shifting to the near-UV band over time. The peak frequency decreases and the spectral magnitude diminishes as ϵ_{rad} decreases. Model IV shows a higher peak at a higher frequency compared to Model III due to the non-zero positive value of $\bar{\alpha}_{z\phi}$, which increases the radiative flux as shown in equation (12), resulting in a brighter spectral luminosity for the disk.

Figure 11 shows the bolometric luminosities and the disk luminosities of the X-ray, UV, and optical bands calculated by equation (28). As shown in panel (a), the bolometric light curves, L_{b} , are smaller than the Eddington luminosity (see equation 23) for all models over the long-term evolution. From the remaining panels, we see that for all models, the UV band luminosity is the brightest among the three bands. The X-ray luminosity varies significantly with time for all models, as shown in panel (b), while the optical and UV luminosities increase with time before $t/\tau_0 = 1.0$ and then decrease rapidly at later times due to the wind-driven disk mass depletion, as shown in panels (c) and (d). The bolometric light curves show a more gradual but similar temporal variability to the X-ray light curves.

As shown in panel (b) of Figure 11, the X-ray luminosity decreases with time at early stages and increases rapidly around $t/\tau_0 \sim 1.0$. This re-brightening occurs as the mass in the disk starts to accrete onto the black hole due to the viscous spreading of the initial Gaussian ring. In fact, the time corresponding to the peak of the X-ray re-brightening coincides with the peak time of the mass accretion rate, as seen in Figure 7. After the peak, the surface density near the inner radius decreases due to accretion and mass loss, resulting in a rapid decrease in luminosity. In contrast, the optical and UV luminosities increase with time at early stages. This is because the disk spectrum, as the initial

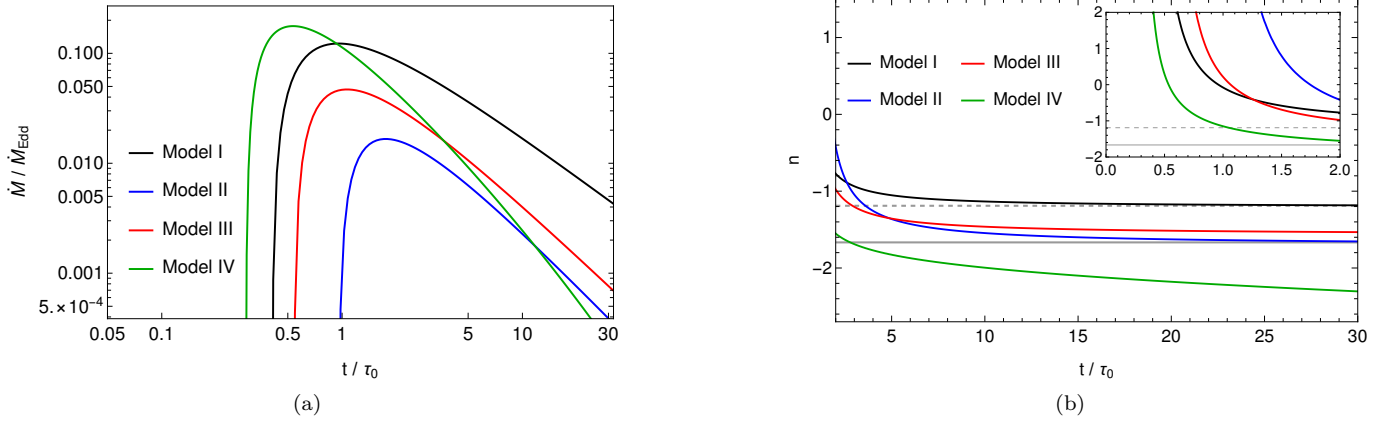


Figure 7. Time evolution of the mass accretion rates estimated at the disk’s inner radius for all models, along with the corresponding slopes. In panel (a), the mass accretion rate is normalized by the Eddington accretion rate. Different line colors represent different models. In panel (b), the slope is represented by the power-law index of time. The gray solid and dashed lines correspond to $-5/3$ (mass fallback rate case; Lodato et al. 2009) and $-19/16$ (classical solution case; Cannizzo et al. 1990), respectively. The inset plot displays the slope at early times.

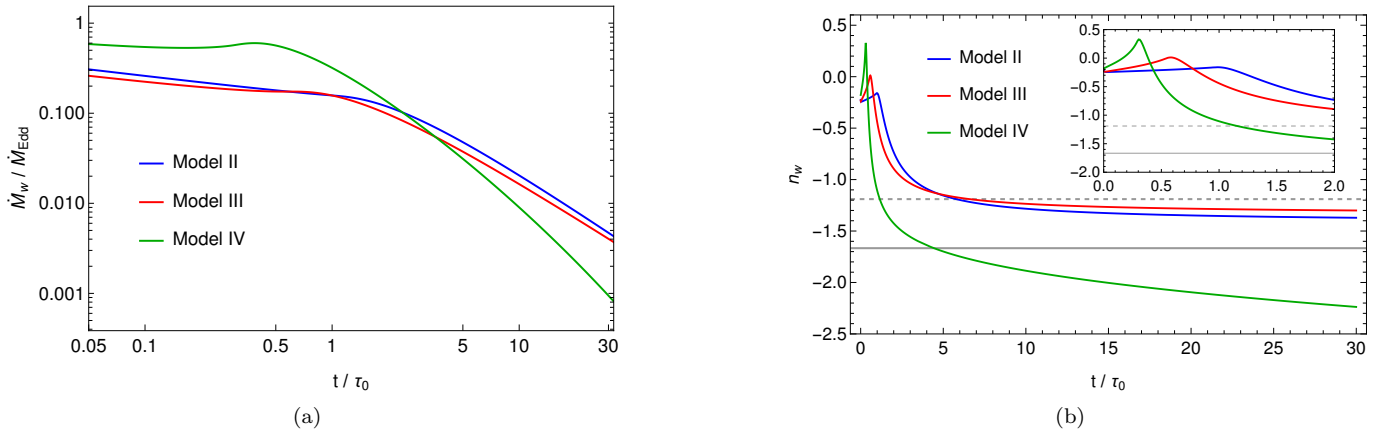


Figure 8. Same format as Figure 7, but for the mass loss rates for Models II through IV. Note that there is no mass loss in Model I.

Gaussian ring viscously spreads, peaks around the optical to UV range. After reaching the peaks, these luminosities decrease with time.

The comparison between Model IV and the other three models shows that the spectral luminosity for a non-zero $\bar{\alpha}_{z\phi}$ increases significantly at early times but decreases rapidly at late times compared to the cases of $\bar{\alpha}_{z\phi} = 0$. This is due to the high rate of mass accretion and loss for $\bar{\alpha}_{z\phi} = 0.001$, which promotes efficient depletion of the disk mass, quickly leading to a low disk surface density and temperature at late times compared to other cases.

The X-ray luminosity is negligibly small for Model II, i.e., the case of the low value of ϵ_{rad} with $\bar{\alpha}_{z\phi} = 0$. Comparing Models III and IV, we find that the non-zero value of $\bar{\alpha}_{z\phi}$ increases the X-ray luminosity by more than two orders of magnitude. This suggests that magnetic braking plays an important role in mass accretion from the outer to the inner radius.

3.4. ϵ_{rad} -dependence of mass loss rates and power-law indices

Figure 12 shows the dependence of the mass loss rates on ϵ_{rad} at three different times for $\bar{\alpha}_{z\phi} = 0$. The mass loss rate decreases with time, as expected. The mass loss rates peak around $\epsilon_{\text{rad}}=0.2$ at three different times. According to equation (15), $C_{w,0}$ and the energy available for mass loss are higher for smaller ϵ_{rad} , suggesting that the mass loss

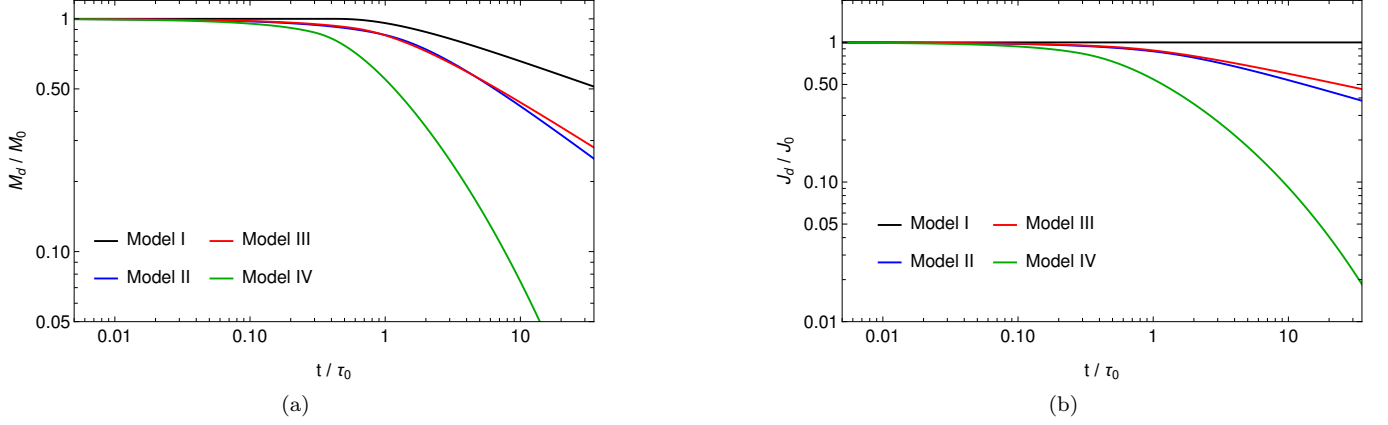


Figure 9. Time evolution of the disk mass and angular momentum for Models I through IV. The different colors represent the different models. The disk mass is normalized by the mass of the bound debris, given by $M_0 = M_*/2 \sim 1.0 \times 10^{33} \text{ g}$ (M_*/M_\odot). The normalization of the disk angular momentum is determined by the angular momentum of the bound debris, $J_0 = M_0 \sqrt{2GM\tau_t} \sim 4.3 \times 10^{55} \text{ g cm}^2 \text{ s}^{-1}$.

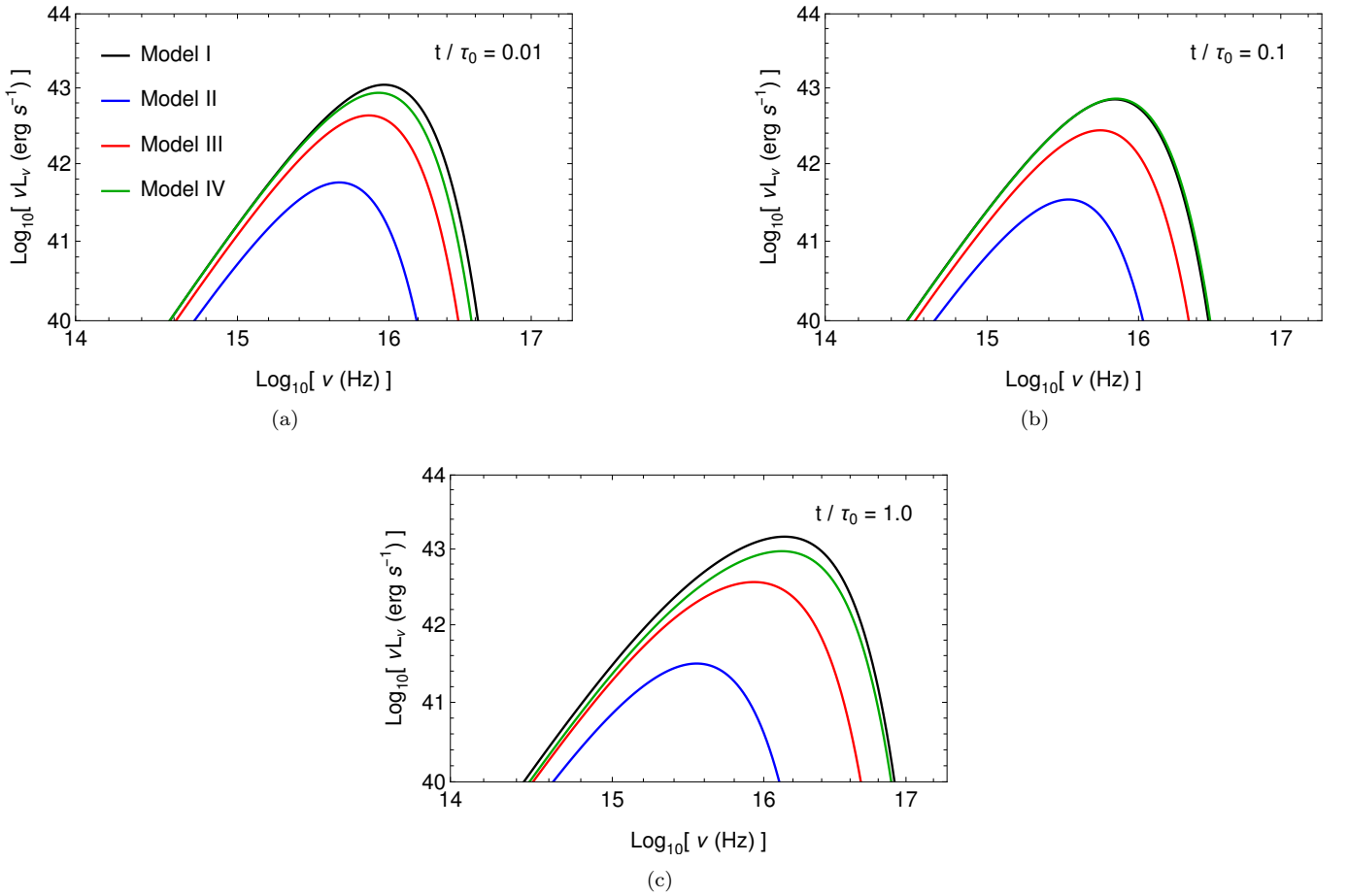


Figure 10. Frequency distributions of the spectral luminosities (see equation 29) for Models I through IV. Different models are represented in different colors. Panels (a), (b), and (c) display the $t/\tau_0 = 0.01$ case, the $t/\tau_0 = 0.1$ case, and the $t/\tau_0 = 1.0$ case, respectively.

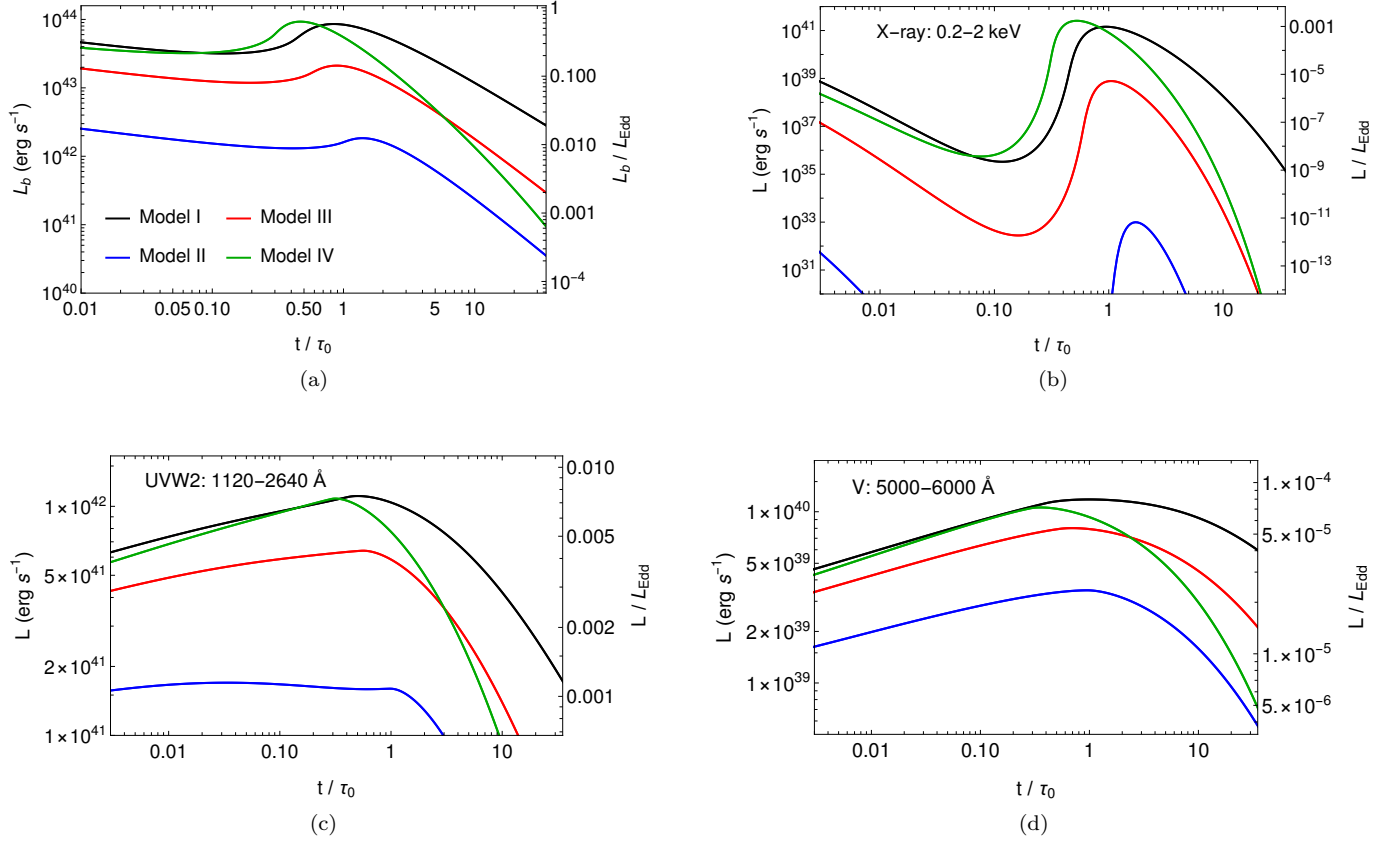


Figure 11. Time evolution of the disk luminosities of the three spectral bands and the bolometric luminosities for Models I through IV. Panels (a), (b), (c), and (d) show bolometric and three luminosities (X-ray, UV, and optical). Different colors indicate different models in all the panels.

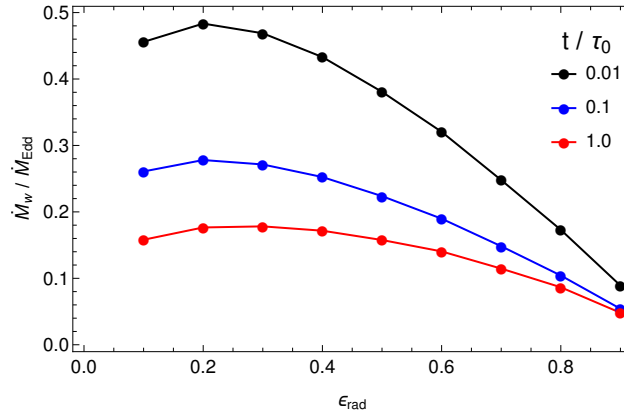


Figure 12. ϵ_{rad} -dependent mass loss rates at the three different times for $\bar{\alpha}_{z\phi} = 0$. Different colors indicate those different times. The mass loss rates are normalized by the Eddington accretion rate, \dot{M}_{Edd} . The filled circle represents each data point in every $\epsilon_{\text{rad}} = 0.1$ step.

rate is highest at the zero cooling limit, i.e., at $\epsilon_{\text{rad}} = 0$. However, one can see a local maximum in the mass loss rate at $\epsilon_{\text{rad}} \approx 0.2$. This is because the surface density and temperature of smaller ϵ_{rad} cases are lower than those of larger ϵ_{rad} cases, particularly in the inner region. One may find this tendency in panels (a) and (b) of Figure 2; the surface density of Model II ($\epsilon_{\text{rad}} = 0.1$) is considerably lower than that of Model III ($\epsilon_{\text{rad}} = 0.5$) in $r/r_g \lesssim 50$ due to the more efficient mass removal by the disk wind. Consequently, the temperature is also lower because of the reduced accretion

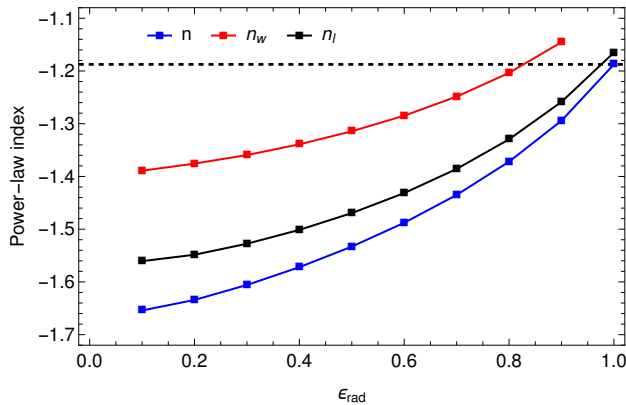


Figure 13. ϵ_{rad} -dependence of the slopes of mass accretion and loss rates for $\bar{\alpha}_{z\phi} = 0$. For all the cases, n , n_w , and n_l are evaluated at $t/\tau_0 = 30$ and are denoted by blue, red, and black solid lines, respectively. Each data point in every $\epsilon_{\text{rad}} = 0.1$ step is indicated by the filled square. The horizontal black dashed line indicates the no wind case ($n = -19/16$) as a fiducial value (Cannizzo et al. 1990).

heating. The lower surface density and temperature lead to the smaller mass flux of the disk wind (see equation 5). Therefore, the total mass loss rate decreases for $\epsilon_{\text{rad}} \rightarrow 0$ in the small ϵ_{rad} ($\lesssim 0.2$) regime.

It is not trivial that the bolometric luminosity is proportional to the mass accretion rate if the mass loss by the disk wind is present. The power-law index of the bolometric lightcurve is defined by

$$n_l = \frac{d \ln(L_b)}{d \ln t},$$

where L_b is given by equation (28) with $\nu_l = 0$ and $\nu_u = \infty$. For comparison purposes, we show ϵ_{rad} -dependence of power law indices: n , n_w , and n_l at a sufficiently late time, $t/\tau_0 = 30$, in Figure 13. It is noted from the figure that $|n|$ is higher than $|n_w|$ and $|n_l|$ takes a value between $|n|$ and $|n_w|$ in the reasonable range of ϵ_{rad} . The steeper slope of the mass accretion rate indicates that it declines more rapidly than the mass loss rate by the disk wind and that the former is dominated by the latter at the late phase. This is because the disk wind removes the gas from early times so that the surface density in the inner region is lower for smaller ϵ_{rad} as shown in Figure 2 (a). Since the mass accretion rate is proportional to the surface density at the inner disk edge, it drops more rapidly with time for smaller ϵ_{rad} , which gives larger $|n|$ as shown in Figure 13. In contrast, the decrease in the mass loss rate is slower because disk winds still emanate from the outer region where sufficient mass remains. It results in moderately smaller $|n_w|$. Panel (d) of Figure 4 supports this interpretation. Considering the bolometric luminosity is affected through Q_{rad} (see equation 7) by both mass accretion and mass loss, it is natural that the resultant power-law index of the bolometric luminosity has some value between $|n|$ and $|n_w|$ for the given range of ϵ_{rad} . As ϵ_{rad} is larger, n_l asymptotes n . A slight deviation yet exists between n and n_l even if the disk wind is absent ($\epsilon_{\text{rad}} = 1$). This is because of the time-dependent nature of the accretion disk. In fact, we confirm that n_l corresponds to n in the steady-state limit ($t/\tau_0 \simeq 100$).

3.5. Impact of the initial disk mass

The peak of the initial radial distribution of the surface density, Σ_0 , increases with the initial disk mass M_i , as seen in equation (18), which increases the mass accretion and loss rates. Figures 4 and 5 show that the mass accretion rate initially exceeds the Eddington accretion rate, indicating that the initial disk with a ring-like structure is a radiation-pressure dominated, super-Eddington accretion flow. Subsequently, the disk viscously spreads with time to begin accreting onto an SMBH at a sub-Eddington accretion rate after $t/\tau_0 > 0.5$, indicating that our formulation is adequate after that time. However, our formulation is insufficient to describe the structure and evolution of the super-Eddington flow at a very early time. Therefore, we explore the effect of the initial disk mass, M_i , on the mass accretion and loss rates at late times by comparing the disk model with a much lower initial mass $M_i = 0.005M_\odot$.

Figure 14 compares the mass accretion rate of $M_i = 0.5M_\odot$ with that of $0.005M_\odot$ at $t/\tau_0 = 0.001$. It is noted from the figure that the mass accretion rate for the $M_i = 0.005$ case is at a sub-Eddington rate from the beginning. Figure 15 shows the radiation-to-gas pressure ratio in the disk for Models I to IV. The radiation pressure is dominant for the $M_i = 0.5M_\odot$ case, while the gas pressure is dominant for the $M_i = 0.005M_\odot$ case. From equations (7), (12), and (16), the ratio of radiation pressure to gas pressure is given as $p_{\text{rad}}/p_{\text{gas}} \propto \epsilon_{\text{rad}}[(3/2)\bar{\alpha}_{r\phi}(H/r) + \bar{\alpha}_{z\phi}/2]r\Omega\Sigma$, where $p_{\text{rad}} \propto T^4$. Note that the surface density decreases as the initial disk mass decreases. When the initial disk mass is extremely low, the contribution of the $\bar{\alpha}_{z\phi}$ term to $p_{\text{rad}}/p_{\text{gas}}$ becomes larger than that of the $\bar{\alpha}_{r\phi}$ term for moderate values of ϵ_{rad} . As a result, $p_{\text{rad}}/p_{\text{gas}}$ is larger in magnitude in Model IV than in Model I, as shown in panel (b) of Figure 15. Figures 14 and 15 demonstrate that the disk with $M_i = 0.005M_\odot$ is a geometrically thin, gas-pressure dominant.

The viscous timescale of a geometrically thin, gas-pressure dominated disk is proportional to $\Sigma^{-2/3}$, and the initial surface density is proportional to M_i . Therefore, the viscous timescale is longer for disks with lower initial mass. As a result, the disk with $M_i = 0.005M_\odot$ evolves much more slowly than the disk with $M_i = 0.5M_\odot$ over the course of the calculation. Panels (a) and (b) of Figure 16 show the time evolution of the mass accretion rates at the ISCO radius for all four models, along with the corresponding mass loss rates. As predicted, in the case of $M_i = 0.005M_\odot$, the peak mass accretion rate is much lower, and the time at which this peak occurs is significantly delayed compared to the case of $M_i = 0.5M_\odot$. Similarly, the mass loss rate for the $M_i = 0.005M_\odot$ case is significantly lower. This lower outflow rate and longer viscous timescale extend the duration of the early, flatter phase of the mass loss rate compared to the $M_i = 0.5M_\odot$ case.

Figure 17 shows the time evolution of the power law indices of time of the mass accretion and loss rates, which are given by equations (25) and (26), respectively. The n and n_w reach the same saturation value at the late times for $M_i = 0.5M_\odot$ and $0.005M_\odot$ for Models I, II, and III. In contrast, the n and n_w of Model IV corresponding to the non-zero value of $\bar{\alpha}_{z\phi}$, decrease more rapidly at late times for $M_i = 0.005M_\odot$ than for $M_i = 0.5M_\odot$. These results indicate that no initial disk mass impacts the late-time evolution of the disk without magnetic braking, while the initial disk mass affects the late-time evolution of the disk wind with magnetic braking.

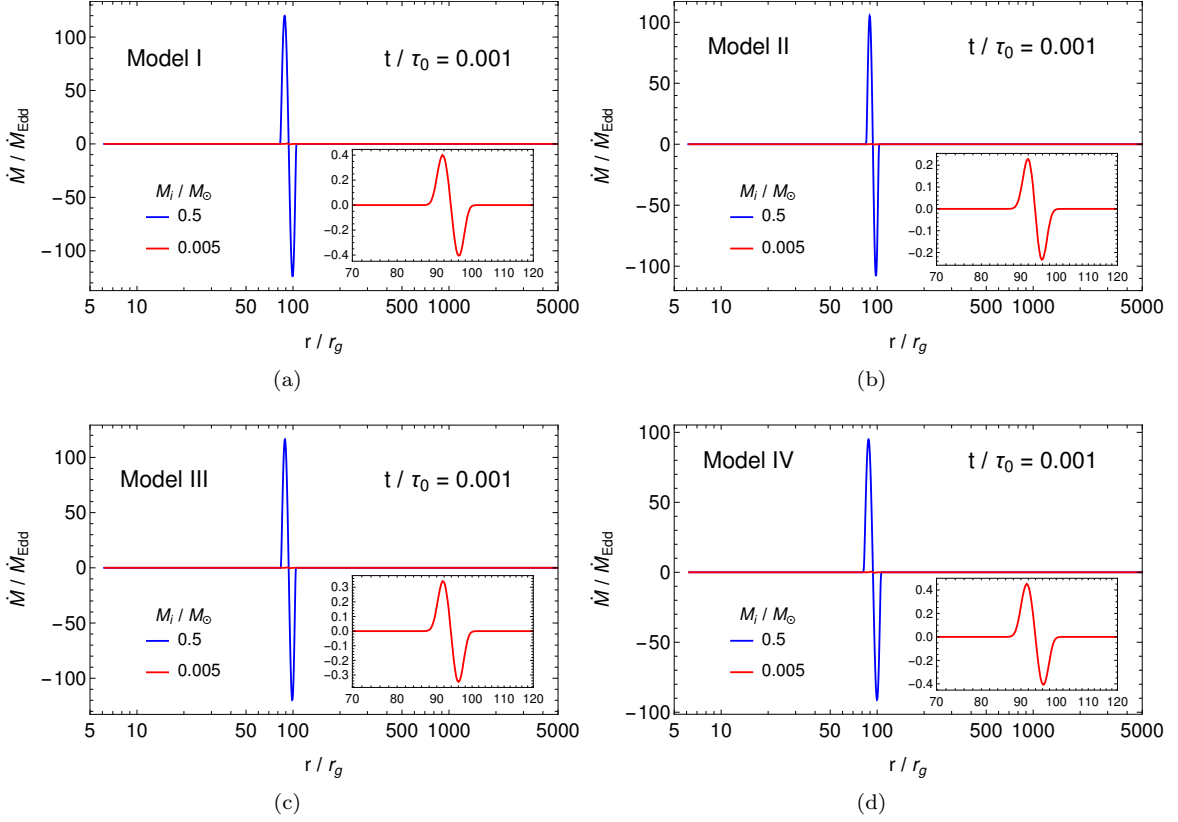


Figure 14. Radial profiles of the mass accretion rates, which are obtained by equation (20), at a near initial time $t/\tau_0 = 0.001$. Panels (a) to (d) represent those of Model I to IV. For all panels, the blue and red solid lines correspond to an initial disk mass of $M_i = 0.5M_\odot$ and $0.005M_\odot$, respectively. The mass accretion and loss rates are normalized by the Eddington accretion rate.

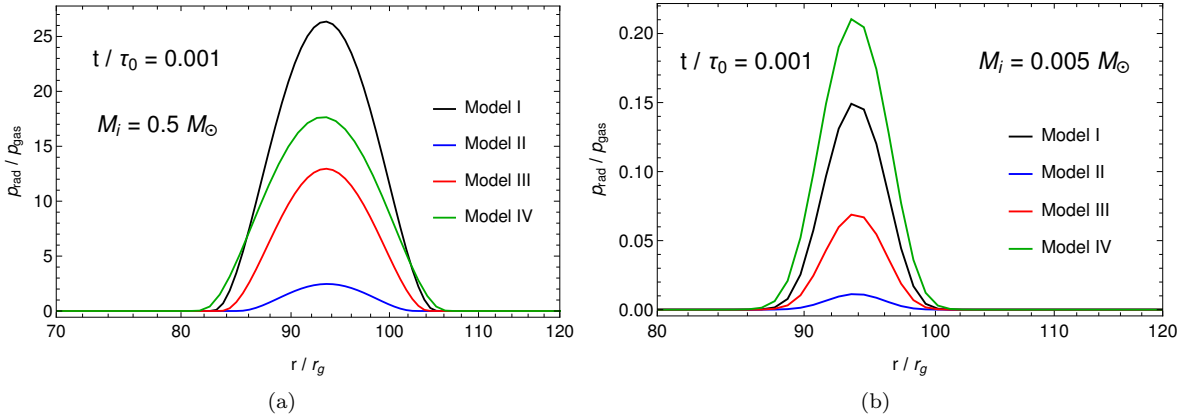


Figure 15. Radial profile of the radiation to gas pressure ratio for Models I to IV at a near initial time $t/\tau_0 = 0.001$. Panels (a) and (b) correspond to an initial disk mass of $M_i = 0.5M_\odot$ and $0.005M_\odot$, respectively. In both panels, the different colored lines indicate different models.

4. DISCUSSION

We have derived the basic equations for a time-dependent, one-dimensional, magnetically driven disk-wind model based on magnetohydrodynamic (MHD) equations in the context of TDEs and present a particular solution for these equations. We initiate our calculations with the initial condition that the surface density is Gaussian-distributed around the circularization radius. Four key parameters characterize the subsequent evolution of the disk and wind:

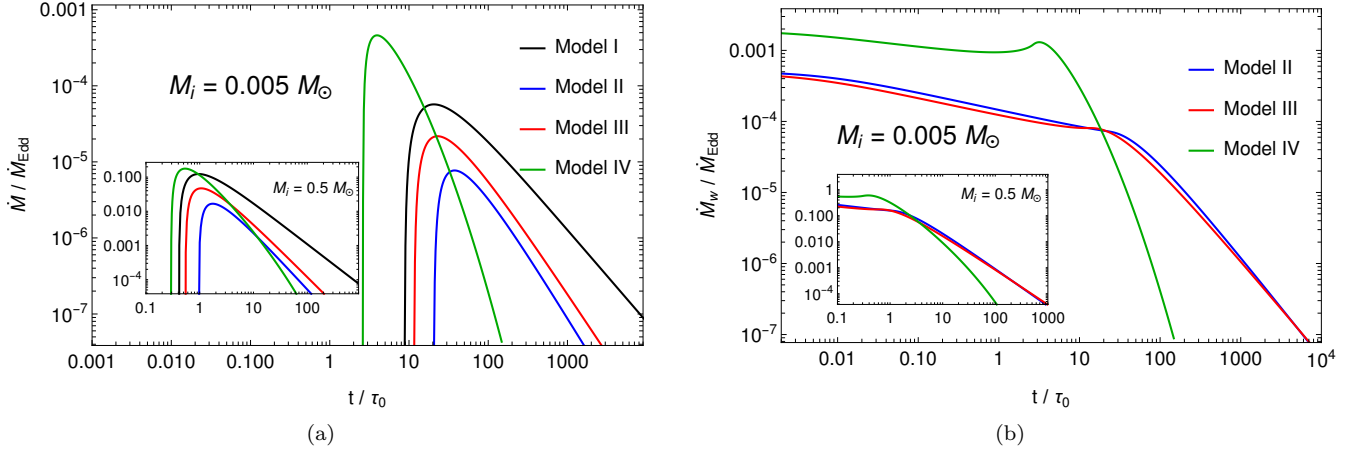


Figure 16. Time evolution of the mass accretion rate estimated at the ISCO radius and the mass loss rate for the case of $M_i = 0.005 M_\odot$. Panels (a) and (b) represent the mass accretion rate curve and the mass loss rate curve for all four models, respectively. The different colored lines indicate different models. The Eddington accretion rate normalizes both the mass accretion and loss rates. The insets of panels (a) and (b) display the mass accretion and loss rates for the $M_i = 0.5 M_\odot$ case, respectively.

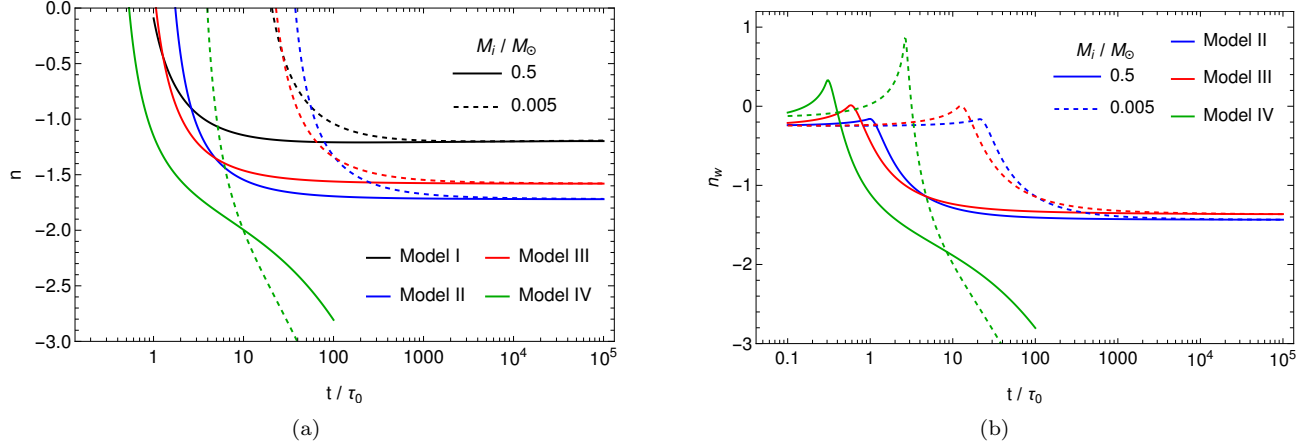


Figure 17. Time evolution of the power-law indices of the mass accretion rate and mass loss rate curves. The indices n and n_w are given by equations (25) and (26), respectively. The solid and dashed lines correspond to the cases $M_i = 0.5 M_\odot$ and $0.005 M_\odot$, respectively. The different colored lines indicate different models.

($\bar{\alpha}_{r\phi}$, $\bar{\alpha}_{z\phi}$, ϵ_{rad} , $C_{w,0}$). The first two parameters are introduced by extending the α parameter prescription, while the remaining two parameters, ϵ_{rad} and $C_{w,0}$, are introduced to close the basic equations and to control the vertical mass flux, respectively.

The viscosity parameter $\bar{\alpha}_{r\phi}$ corresponds to the Shakura-Sunyaev viscosity parameter $\alpha = 2\bar{\alpha}_{r\phi}/3$ for pure hydrodynamics. In fact, the first term on the right-hand side of equation (12) reduces to the viscous heating rate of the standard disk model for $\bar{\alpha}_{z\phi} = 0$, $C_{w,0} = 0$, and $\epsilon_{\text{rad}} = 1$. In our model, we used $\bar{\alpha}_{r\phi} = 0.1$, which corresponds to $\alpha \approx 0.067$. Starling et al. (2004) estimated $0.01 \leq \alpha \leq 0.03$ from the optical variabilities on timescales of months to years for 41 quasars. This range of α is within the range of ~ 0.005 to ~ 0.6 predicted by various local shearing box MHD turbulent disk simulations (Hawley et al. 1995; Matsumoto & Tajima 1995; Brandenburg et al. 1995; Gogichaishvili et al. 2018).

In our model, a part of disk heating due to the viscosity and magnetic braking goes to radiative cooling. The assigned energy to the cooling is controlled by an unknown parameter, ϵ_{rad} (see equation 12). For given C_w , we can evaluate

ϵ_{rad} by equations (15) and (24) as

$$\epsilon_{\text{rad}} = 1 - \frac{C_{\text{w},0}}{2} \left[3\bar{\alpha}_{r\phi} \left(\frac{H}{r} \right)^2 + \bar{\alpha}_{z\phi} \left(\frac{H}{r} \right) \right]^{-1}.$$

For $C_{\text{w},0} = 1.0 \times 10^{-5}$, $\bar{\alpha}_{r\phi} = 0.1$, and $H/r = 5 \times 10^{-3}$, we estimate $\epsilon_{\text{rad}} \approx 1/3$ for $\bar{\alpha}_{z\phi} = 0$ and $\epsilon_{\text{rad}} \approx 0.6$ for $\bar{\alpha}_{z\phi} = 0.001$. By obtaining C_{w} from the local MHD simulations, we can solve a set of basic equations without ϵ_{rad} . To obtain the vertical velocity directly without introducing C_{w} , we need to add the vertical component of the momentum conservation equation in the current basic equations and solve it simultaneously. This is our future work.

Adopting $\bar{\alpha}_{r\phi} = 0.1$, $\bar{\alpha}_{z\phi} = 0$, and $H/r = 5 \times 10^{-3}$, we obtain $C_{\text{w},0} \sim 1.5 \times 10^{-5}(1 - \epsilon_{\text{rad}})$ from equation (24), which corresponds to a plasma beta of $\mathcal{O}(10)$ (Suzuki et al. 2010) when $\epsilon_{\text{rad}} \ll 1$, indicating a strong magnetic field. According to Suzuki & Inutsuka (2009); Suzuki et al. (2010), $C_{\text{w},0}$ becomes larger as the plasma beta decreases. Since the effect of the disk wind is negligible if the magnetic field is such weak that $C_{\text{w}} \ll 1.5 \times 10^{-5}$, i.e., $\epsilon_{\text{rad}} \sim 1$, we expect the power-law index to have asymptotes $n = -19/16$. Next, the power-law index is distributed over $-5/3 \lesssim n < -19/16$ when the magnetic field is mildly strong, corresponding to $C_{\text{w},0} \lesssim 1.5 \times 10^{-5}$, i.e., $\epsilon_{\text{rad}} < 1$. This case is consistent with ASASSN-18pg, whose bolometric luminosity at late times is flatter than $t^{-5/3}$ (Holoien et al. 2020). Note that $\epsilon_{\text{rad}} = 0$ gives an upper limit of $C_{\text{w},0}$, meaning that $C_{\text{w},0}$ is not greater than 1.5×10^{-5} with the current parameter sets. However, $C_{\text{w},0}$ can be greater than 1.5×10^{-5} if $\bar{\alpha}_{z\phi}$ takes a non-zero value, indicating a magnetic field strong enough for magnetic braking to work efficiently. This scenario can explain the late-time variation of the following TDEs: AT2019qiz, whose light curve decays rapidly with time, scaling as $t^{-2.54}$ (Nicholl et al. 2020), and possibly ASASSN-14ae and ASASSN-15oi, whose light curves exhibit an exponential decline at late times (Holoien et al. 2014, 2016). We have discovered a new regime of power-law indices at late times: $-5/3 \lesssim n < -19/16$ for $\bar{\alpha}_{z\phi} = 0$ or $n < -2$ for $\bar{\alpha}_{z\phi} > 0$. Our MHD disk-wind model naturally explains TDEs that deviate from the late-time light curves of X-ray TDEs, whose power-law index follows $n \lesssim -1.2$ as described in Auchettl et al. (2017).

As described in section 3.5, if the initial disk mass is large, the accretion rate can exceed the Eddington limit during the early stages, prior to accretion onto the black hole. In the absence of magnetic braking, this excess does not significantly impact the late-time evolution of the accretion and mass loss rates. However, when magnetic braking is considered, it influences their subsequent evolution. In the super-Eddington accretion flow, a radiation pressure is dominant and the advection cooling term is significant in the energy equation, which is different from the geometrically thin disk case that we assume throughout this paper (Abramowicz et al. 1988; Frank et al. 2002; Kato et al. 2008; Xue et al. 2011). It is interesting how advection cooling and radiation pressure change the physical properties of the magnetically driven disk wind. Therefore, in the future we will reformulate the basic equations for the current time-dependent model accordingly and specifically investigate the case of non-zero value of $\alpha_{z\phi}$.

We ideally need to perform multi-dimensional MHD simulations of the evolution of the MHD disk-wind system for deciding all the parameters, including the remaining $\bar{\alpha}_{r\phi}$ and $\bar{\alpha}_{z\phi}$. Especially, the magnetic field geometry of the accretion disk is so complicated that deciding the reasonable magnetic field geometry over the long term is challenging (Jafari & Vishniac 2018). Thus, some assumptions are yet needed to decide it. Li & Cao (2019) constructed a steady disk-outflow model in which the large-scale field forms by the advection of the external field in the disk. They showed that a moderate external field (plasma beta of several hundred at the outer disk radius) leads to a large-scale magnetic field inclined with the disk surface and supports the disk outflow. They found that the outflow is non-relativistic overall and the terminal velocity of the outflow emitted from the disk's inner radius is up to $\sim 0.3 c$, and the mass loss rate can be higher than the mass accretion rate for a certain range of the plasma beta. As seen in Figures 4 and 5, our time-dependent model also demonstrates that the mass outflow rate is higher than the mass accretion rate, although their time evolution can change by ϵ_{rad} , $\bar{\alpha}_{r\phi}$ and $\bar{\alpha}_{z\phi}$. For exploring the plasma-beta dependence on this result, we need to decide on the magnetic field evolution. We will extend our time-dependent model by solving the induction equation in the future.

There are some X-ray TDEs, such as ASASSN-15oi (Gezari et al. 2017), OGLE16aaa (Kajava et al. 2020), and AT 2019azh (Liu et al. 2022), which show the late-time X-ray brightening with the optical and UV flares at early times. OGLE16aaa was not detected in the soft X-ray waveband at discovery, while ASASSN-15oi and AT2019azh were also detected at early times. This early-time X-ray emission is very weak at 10^{41} erg/s. In contrast, the late-time X-ray luminosity is one or two orders of magnitude higher to be 10^{42-43} erg/s, but still significantly lower than the early-time optical and UV luminosities. Hayasaki & Jonker (2021) proposed the simple analytical model that the late-time X-ray flare is caused by the viscous accretion from the disk circularization, while the optical and UV flares occurs due to

the stream-stream collision at early times. The time in our model is normalized by a viscous timescale $\tau_0 = 14.3$ yr. The X-ray brightens at $t/\tau_0 \lesssim 1$ for Models I, II, and III, while it brightens at $t/\tau_0 < 1$ in Model IV because magnetic braking (non-zero value of $\bar{\alpha}_{z\phi}$) causes faster accretion due to the shorter viscous timescale. In addition, Models I and IV show that the X-ray luminosity has a peak of $\sim 10^{41}$ erg/s from panel (b) of Figure 11. These results indicate that Model IV can explain the observed X-ray rebrightening. The X-ray luminosity is still low compared to the observed one, but, e.g., higher values of ϵ_{rad} and $\bar{\alpha}_{z\phi}$ would allow for higher luminosity. The detailed comparison between our model and the observed X-ray rebrightening is our future task.

Several TDEs such as PS1-10jh (Gezari et al. 2012), ASASSN-14ae (Holoien et al. 2014), OGLE16aaa (Wyrzykowski et al. 2017), iPTF16axa (Hung et al. 2017), iPTF16fnl (Blagorodnova et al. 2017), AT2017eqx (Nicholl et al. 2019), AT2019qiz (Nicholl et al. 2020), and ASASSN-18pg (Holoien et al. 2020) has been shown to have significantly brighter optical and UV emissions compared to its observationally insignificant X-ray emissions. The strong dominance of optical and UV radiation in the observational spectrum is interpreted by the disk-wind model, in which an optically thick outflow obscures the disk emission, and the emitted X-ray photons are reprocessed into lower-energy optical or UV photons (Roth et al. 2020). A spherical outflow model from a super-Eddington accretion flow has been constructed for TDEs by Strubbe & Quataert (2009); Piro & Lu (2020); Mageshwaran et al. (2023). Following these studies, assuming a spherically symmetric wind launched from a radius r_1 with a mass loss rate \dot{M}_w , wind velocity v_w , and wind density $\rho(r) = \rho_1(r/r_1)^{-2}$, where $\rho_1 = \dot{M}_w/4\pi r_1^2 v_w$, we can estimate the optical depth of the wind as

$$\begin{aligned} \tau(r) &= \int_r^{r_{\text{out}}} \rho \kappa_{\text{es}} \, dr = \frac{\kappa_{\text{es}} \dot{M}_w}{4\pi r_1 v_w} \left(\frac{r}{r_1}\right)^{-1} \\ &\sim 50 \left(\frac{\dot{M}_w}{\dot{M}_{\text{Edd}}}\right) \left(\frac{v_w}{10^4 \text{ km s}^{-1}}\right)^{-1} \left(\frac{r_1}{r_{\text{ISCO}}}\right)^{-1} \left(\frac{r}{r_l}\right)^{-1}, \end{aligned}$$

where we also assumed that $r_{\text{out}} \gg r_1$. If $\dot{M}_w \ll \dot{M}_{\text{Edd}}$, the wind is optically thin, and thus reprocessing is inefficient. This corresponds to cases where the initial disk mass is small or in the later times of our models. In contrast, if $\dot{M}_w \gtrsim \dot{M}_{\text{Edd}}$, the wind is optically thick so that X-ray photons emitted from the disk would be absorbed and re-emitted in the lower energy band. However, we cannot quantitatively evaluate the reprocessed spectrum without solving the radiative transport equation. This is a future task that we will explore.

5. CONCLUSIONS

We have constructed a one-dimensional model of a time-dependent, geometrically thin accretion disk with a magnetically driven non-relativistic wind. The MHD turbulent viscosity and magnetic braking are characterized by two parameters: $\bar{\alpha}_{r\phi}$ and $\bar{\alpha}_{z\phi}$, respectively. These are derived by applying an extended α parameter prescription to the MHD momentum equations. In addition, we have introduced two other parameters: $C_{w,0}$, which controls the vertical mass flux, and ϵ_{rad} , which is the ratio of the thermal cooling flux to the disk heating flux. We have found numerical disk-wind solutions for the basic equations with these four parameters. In the absence of the wind, the angular momentum of the disk is conserved due to the zero viscous torque at the inner boundary. However, the angular momentum decreases with time due to mass loss by the wind. In particular, when magnetic braking is present (i.e., $\bar{\alpha}_{z\phi} \neq 0$), the disk loses angular momentum more efficiently than in the absence of magnetic braking (i.e., $\bar{\alpha}_{z\phi} = 0$). We also confirm that $C_{w,0}$ remains smaller than $C_{w,\text{sim}}$ over the entire disk region within a reasonable time, indicating that the mass flux of the disk wind is determined by the energetic constraint. Our primary conclusions are summarized as follows:

1. The mass accretion rate follows the power law of time $t^{-19/16}$ at late times if the wind is absent ($\epsilon_{\text{rad}} = 1$). This result corresponds to the classical solution of Cannizzo et al. (1990).
2. In the case that the wind is present ($0 < \epsilon_{\text{rad}} < 1$) without magnetic braking ($\bar{\alpha}_{z\phi} = 0$), the mass accretion rate follows the power law of time at late times and is steeper than the classical solution: $t^{-19/16}$. In addition, the mass accretion rate becomes steeper as ϵ_{rad} approaches 0. When magnetic braking is on (i.e., $\bar{\alpha}_{z\phi} = 0.001$), the mass accretion rate decays rapidly with time and the power-law index evolves with time: for $\dot{M} \propto t^n$, $|n|$ becomes larger with time and $n < -2$ at late times.
3. The bolometric luminosity is not proportional to the mass accretion rate due to mass loss by the disk wind. In fact, we find that the bolometric light curve is flatter than the mass accretion rate but steeper than the mass loss

rate in the absence of magnetic braking: the bolometric decay index is distributed over $-5/3 < n_1 \lesssim -19/16$ for $L \propto t^{n_1}$. We also confirm that the bolometric decay index asymptotes to $-19/16$ in the absence of wind at late times.

4. We identify a new regime in the late-time bolometric light curve of a TDE, where it is steeper than the classical $t^{-19/16}$ solution due to magnetically driven winds. For $L \propto t^{n_1}$, we find $-5/3 < n_1 \lesssim -19/16$ in the absence of magnetic braking ($\bar{\alpha}_{z\phi} = 0$), and $n_1 < -2$ when magnetic braking is present ($\bar{\alpha}_{z\phi} \gtrsim 0.001$).
5. In the disk emission, the UV luminosity is the highest among the optical, UV, and X-ray luminosities. The X-ray emission shows a significant rebrightening at late times. In particular, for $\bar{\alpha}_{z\phi} \neq 0$, the X-ray emission reaches the highest peak and exhibits the shortest time interval between the optical or UV and X-ray peaks. These results highlight the critical role of $\bar{\alpha}_{z\phi}$ in modulating the timing and intensity of disk emission, which is of observational importance for understanding the underlying physical mechanisms.
6. Our model predicts that late-time bolometric light curves steeper than $t^{-19/16}$ in UV-bright TDEs are potential evidence for magnetically driven winds.

1 We thank the referee for the constructive suggestions that have improved the paper. M.T. and K.H. have been
2 supported by the Basic Science Research Program through the National Research Foundation of Korea (NRF) funded
3 by the Ministry of Education (2016R1A5A1013277 to K.H. and 2020R1A2C1007219 to K.H. and M.T.). This work was
4 financially supported by the Research Year of Chungbuk National University in 2021. This work is also supported by
5 Grant-in-Aid for Scientific Research from the MEXT/JSPS of Japan, 22H01263 to T.K.S. This research was supported
6 in part by grant no. NSF PHY-2309135 to the Kavli Institute for Theoretical Physics (KITP).

APPENDIX

A. DERIVATION OF BASIC EQUATIONS FOR MHD DISK AND WIND EVOLUTION

In Appendix, we introduce the detailed derivation of the evolutionary equations for the mass and energy of a disk with the wind by adding in the formalism of [Suzuki et al. \(2016\)](#), a modification so as to fit our problem for TDE disks.

A.1. Surface Density Evolution

The mass conservation and momentum conservation equations of the general magneto-hydrodynamics (MHD) are given by ([Balbus & Hawley 1998](#)) as

$$\frac{\partial \rho}{\partial t} + \vec{\nabla} \cdot (\rho \vec{v}) = 0 \quad (\text{A1})$$

and

$$\rho \frac{\partial \vec{v}}{\partial t} + (\rho \vec{v} \cdot \vec{\nabla}) \vec{v} = -\vec{\nabla} \left(p + \frac{B^2}{8\pi} \right) - \rho \vec{\nabla} \Phi + \left(\frac{\vec{B}}{4\pi} \cdot \vec{\nabla} \right) \vec{B} + \eta_v \left(\nabla^2 \vec{v} + \frac{1}{3} \vec{\nabla} (\vec{\nabla} \cdot \vec{v}) \right), \quad (\text{A2})$$

respectively, where \vec{v} is the fluid velocity, p is the pressure,

$$\Phi = -\frac{GM}{\sqrt{r^2 + z^2}} \quad (\text{A3})$$

is the gravitational potential, B is the magnetic-field vector, and η_v is the microscopic kinematic shear viscosity. [Balbus & Hawley \(1998\)](#) assumed that the bulk viscosity due to the microscopic kinematic shear viscosity η_v vanishes.

Assuming that the disk and wind are axisymmetric, we rewrite equations [A1](#) and [A2](#) with cylindrical coordinates as

$$\frac{\partial \rho}{\partial t} + \frac{1}{r} \frac{\partial}{\partial r} (r \rho v_r) + \frac{\partial}{\partial z} (\rho v_z) = 0, \quad (\text{A4})$$

and

$$\frac{\partial}{\partial t} (r \rho v_\phi) + \frac{1}{r} \frac{\partial}{\partial r} \left[r^2 \left\{ \rho v_r v_\phi - \frac{B_r B_\phi}{4\pi} \right\} \right] + \frac{\partial}{\partial z} \left[r \left\{ \rho v_z v_\phi - \frac{B_z B_\phi}{4\pi} \right\} \right] = 0, \quad (\text{A5})$$

respectively.

For the purpose of adopting the α prescription (Shakura & Sunyaev 1973) for our model, we decompose the azimuthal velocity, v_ϕ , into the mean Keplerian flow and perturbation components as

$$v_\phi = r\Omega + \delta v_\phi, \quad (\text{A6})$$

where $\delta v_\phi \ll r\Omega$ and Ω is the Keplerian frequency:

$$\Omega = \sqrt{\frac{GM}{r^3}}. \quad (\text{A7})$$

Note that $\Phi = -r^2\Omega^2$ at the disk mid-plane ($z = 0$) from equation (A3). In addition, we vertically integrate equations (A4) and (A5) to get

$$\frac{\partial \Sigma}{\partial t} + \frac{1}{r} \frac{\partial}{\partial r} (r\Sigma v_r) + \dot{\Sigma}_w = 0 \quad (\text{A8})$$

and

$$\frac{\partial}{\partial t} (r^2\Omega\Sigma) + \frac{1}{r} \frac{\partial}{\partial r} [r^2\Sigma \{v_r r\Omega + \bar{\alpha}_{r\phi} c_s^2\}] + r [\dot{\Sigma}_w r\Omega + \bar{\alpha}_{z\phi} \rho c_s^2] = 0, \quad (\text{A9})$$

where

$$\dot{\Sigma}_w = 2\rho v_{z,H} \quad (\text{A10})$$

is the vertical mass flux, $v_{z,H} \equiv v_z(r, H)$ is the vertical velocity evaluated at the disk scale-height H , and $\bar{\alpha}_{r\phi}$ and $\bar{\alpha}_{z\phi}$ are defined by

$$\bar{\alpha}_{r\phi} \equiv \frac{1}{c_s^2} \int_{-H}^H \rho \left[v_r \delta v_\phi - \frac{B_r B_\phi}{4\pi\rho} \right] dz / \int_{-H}^H \rho dz, \quad (\text{A11})$$

$$\bar{\alpha}_{z\phi} \equiv \frac{1}{c_s^2} \left[v_z \delta v_\phi - \frac{B_z B_\phi}{4\pi\rho} \right]_{z=H}, \quad (\text{A12})$$

respectively.

Equation (A9) is reduced to

$$r\Sigma v_r = -\frac{2}{r\Omega} \left[\frac{\partial}{\partial r} (\bar{\alpha}_{r\phi} r^2 \Sigma c_s^2) + \bar{\alpha}_{z\phi} r^2 \rho c_s^2 \right], \quad (\text{A13})$$

where equations (A7) and (A8) are used for the derivation. Equation (A13) makes it possible to evaluate the mass accretion rate of the disk: $\dot{M} = -2\pi r \Sigma v_r$. Substituting equation (A13) into equation (A8), we obtain the evolutionary equation of the surface density as

$$\frac{\partial \Sigma}{\partial t} - \frac{2}{r} \frac{\partial}{\partial r} \left[\frac{1}{r\Omega} \left\{ \frac{\partial}{\partial r} (\bar{\alpha}_{r\phi} r^2 \Sigma c_s^2) + \bar{\alpha}_{z\phi} r^2 \rho c_s^2 \right\} \right] + \dot{\Sigma}_w = 0, \quad (\text{A14})$$

A.2. Energy Equation

The energy conservation equation is given by (Balbus & Hawley 1998)

$$\frac{\partial}{\partial t} \left[\frac{1}{2} \rho v^2 + \rho\Phi + \frac{p}{\gamma-1} + \frac{B^2}{8\pi} \right] + \vec{\nabla} \cdot \left[\vec{v} \left(\frac{1}{2} \rho v^2 + \rho\Phi + \frac{\gamma}{\gamma-1} p \right) + \frac{\vec{B}}{4\pi} \times (\vec{v} \times \vec{B}) + \vec{Q} \right] = 0,$$

where γ is a ratio of specific heats and $\vec{Q} = (Q_r, Q_\phi, Q_z)$ is other contributions to energy flux in addition to the MHD energy, such as thermal conduction and radiative heating or cooling. The above equation is rewritten in cylindrical coordinates with the axisymmetric assumption as

$$\frac{\partial}{\partial t} \left[\frac{1}{2} \rho v^2 + \rho\Phi + \frac{p}{\gamma-1} + \frac{B^2}{8\pi} \right] + \frac{1}{r} \frac{\partial}{\partial r} \left[r \left\{ v_r \left(\frac{1}{2} \rho v^2 + \rho\Phi + \frac{\gamma}{\gamma-1} p + \frac{B_\phi^2 + B_z^2}{4\pi} \right) - \frac{B_r}{4\pi} (v_\phi B_\phi + v_z B_z) + Q_r \right\} \right]$$

$$+ \frac{\partial}{\partial z} \left[v_z \left(\frac{1}{2} \rho v^2 + \rho \Phi + \frac{\gamma}{\gamma-1} p + \frac{B_\phi^2 + B_r^2}{4\pi} \right) - \frac{B_z}{4\pi} (v_\phi B_\phi + v_r B_r) + Q_z \right] = 0. \quad (\text{A15})$$

Assuming $r\Omega \gg v_r$, δv_ϕ , v_z , c_s , $B/\sqrt{4\pi\rho}$, the second and third terms of equation (A15) are reduced to

$$\frac{\partial}{\partial r} \left[r \left\{ v_r \left(\frac{1}{2} \rho v^2 + \rho \Phi + \frac{\gamma}{\gamma-1} p + \frac{B_\phi^2 + B_r^2}{4\pi} \right) - \frac{B_r}{4\pi} (v_\phi B_\phi + v_z B_z) \right\} \right] = \frac{\partial}{\partial r} \left[r \left\{ -\frac{1}{2} \rho r^2 \Omega^2 v_r + \rho r \Omega \left(v_r \delta v_\phi - \frac{B_r B_\phi}{4\pi\rho} \right) \right\} \right] \quad (\text{A16})$$

and

$$\frac{\partial}{\partial z} \left[v_z \left(\frac{1}{2} \rho v^2 + \rho \Phi + \frac{\gamma}{\gamma-1} p + \frac{B_\phi^2 + B_r^2}{4\pi} \right) - \frac{B_z}{4\pi} (v_\phi B_\phi + v_r B_r) \right] = \frac{\partial}{\partial z} (\rho v_z E_w), \quad (\text{A17})$$

respectively, where equations (A3), (A6), and (A7) are adopted for these modifications, and E_w is given as the wind energy by

$$E_w = \frac{1}{2} v^2 + \Phi + \frac{\gamma c_s^2}{\gamma-1} + \frac{B_\phi^2 + B_r^2}{4\pi\rho} - \frac{B_z}{4\pi\rho v_z} (v_\phi B_\phi + v_r B_r). \quad (\text{A18})$$

Substituting equations (A16) and (A17) into equation (A15), we get

$$\frac{\partial}{\partial t} \left[-\frac{1}{2} \rho r^2 \Omega^2 \right] + \frac{1}{r} \frac{\partial}{\partial r} \left[r \left\{ -\frac{1}{2} \rho r^2 \Omega^2 v_r + \rho r \Omega \left(v_r \delta v_\phi - \frac{B_r B_\phi}{4\pi\rho} \right) \right\} \right] + \frac{\partial}{\partial z} (\rho v_z E_w + Q_z) = 0, \quad (\text{A19})$$

where $Q_r = 0$ is adopted because there is no energy dissipation in the radial direction. Integrating equation (A19) vertically leads to

$$\frac{\partial}{\partial t} \left[-\frac{1}{2} \Sigma r^2 \Omega^2 \right] + \frac{1}{r} \frac{\partial}{\partial r} \left[r \left\{ -\frac{1}{2} \Sigma r^2 \Omega^2 v_r + \bar{\alpha}_{r\phi} \Sigma r \Omega c_s^2 \right\} \right] + \dot{\Sigma}_w E_w + Q_{\text{rad}} = 0, \quad (\text{A20})$$

where $Q_{\text{rad}} = \int_{-H}^H Q_z dz$ is the radiative cooling rate.

Combining equation (A20) with equation (A14) results in

$$\dot{\Sigma}_w \left[E_w + \frac{r^2 \Omega^2}{2} \right] + Q_{\text{rad}} = \frac{3}{2} \bar{\alpha}_{r\phi} \Omega \Sigma c_s^2 + \bar{\alpha}_{z\phi} r \Omega \rho c_s^2, \quad (\text{A21})$$

where equation (A7) is adopted for the derivation.

REFERENCES

- Abramowicz, M. A., Czerny, B., Lasota, J. P., & Szuszkiewicz, E. 1988, *ApJ*, 332, 646, doi: [10.1086/166683](https://doi.org/10.1086/166683)
- Auchettl, K., Guillochon, J., & Ramirez-Ruiz, E. 2017, *ApJ*, 838, 149, doi: [10.3847/1538-4357/aa633b](https://doi.org/10.3847/1538-4357/aa633b)
- Bagnulo, S., Landolfi, M., & Landi Degl'Innocenti, M. 1999, *A&A*, 343, 865
- Balbus, S. A., & Hawley, J. F. 1991, *ApJ*, 376, 214, doi: [10.1086/170270](https://doi.org/10.1086/170270)
- . 1998, *Reviews of Modern Physics*, 70, 1, doi: [10.1103/RevModPhys.70.1](https://doi.org/10.1103/RevModPhys.70.1)
- Blagorodnova, N., Gezari, S., Hung, T., et al. 2017, *ApJ*, 844, 46, doi: [10.3847/1538-4357/aa7579](https://doi.org/10.3847/1538-4357/aa7579)
- Blandford, R. D., & Payne, D. G. 1982, *MNRAS*, 199, 883, doi: [10.1093/mnras/199.4.883](https://doi.org/10.1093/mnras/199.4.883)
- Bonnerot, C., Price, D. J., Lodato, G., & Rossi, E. M. 2017a, *MNRAS*, 469, 4879, doi: [10.1093/mnras/stx1210](https://doi.org/10.1093/mnras/stx1210)
- Bonnerot, C., Rossi, E. M., & Lodato, G. 2017b, *MNRAS*, 464, 2816, doi: [10.1093/mnras/stw2547](https://doi.org/10.1093/mnras/stw2547)
- Bonnerot, C., Rossi, E. M., Lodato, G., & Price, D. J. 2016, *MNRAS*, 455, 2253, doi: [10.1093/mnras/stv2411](https://doi.org/10.1093/mnras/stv2411)
- Brandenburg, A., Nordlund, A., Stein, R. F., & Torkelsson, U. 1995, *ApJ*, 446, 741, doi: [10.1086/175831](https://doi.org/10.1086/175831)
- Cannizzo, J. K., Lee, H. M., & Goodman, J. 1990, *ApJ*, 351, 38, doi: [10.1086/168442](https://doi.org/10.1086/168442)

- Cao, X., & Gu, W.-M. 2015, *MNRAS*, 448, 3514, doi: [10.1093/mnras/stv269](https://doi.org/10.1093/mnras/stv269)
- Chandrasekhar, S. 1961, *Hydrodynamic and hydromagnetic stability* (Oxford University Press)
- Cufari, M., Coughlin, E. R., & Nixon, C. J. 2022, *ApJ*, 924, 34, doi: [10.3847/1538-4357/ac32be](https://doi.org/10.3847/1538-4357/ac32be)
- Curd, B., & Narayan, R. 2019, *MNRAS*, 483, 565, doi: [10.1093/mnras/sty3134](https://doi.org/10.1093/mnras/sty3134)
- . 2023, *MNRAS*, 518, 3441, doi: [10.1093/mnras/stac3330](https://doi.org/10.1093/mnras/stac3330)
- Dai, L., McKinney, J. C., Roth, N., Ramirez-Ruiz, E., & Miller, M. C. 2018, *ApJL*, 859, L20, doi: [10.3847/2041-8213/aab429](https://doi.org/10.3847/2041-8213/aab429)
- Donati, J. F., Babel, J., Harries, T. J., et al. 2002, *MNRAS*, 333, 55, doi: [10.1046/j.1365-8711.2002.05379.x](https://doi.org/10.1046/j.1365-8711.2002.05379.x)
- Feng, J., Cao, X., Gu, W.-M., & Ma, R.-Y. 2019, *ApJ*, 885, 93, doi: [10.3847/1538-4357/ab4592](https://doi.org/10.3847/1538-4357/ab4592)
- Folsom, C. P., Petit, P., Bouvier, J., et al. 2016, *MNRAS*, 457, 580, doi: [10.1093/mnras/stv2924](https://doi.org/10.1093/mnras/stv2924)
- Frank, J., King, A., & Raine, D. J. 2002, *Accretion Power in Astrophysics: Third Edition* (Cambridge University Press)
- Gezari, S., Cenko, S. B., & Arcavi, I. 2017, *ApJL*, 851, L47, doi: [10.3847/2041-8213/aaa0c2](https://doi.org/10.3847/2041-8213/aaa0c2)
- Gezari, S., Chornock, R., Rest, A., et al. 2012, *Nature*, 485, 217, doi: [10.1038/nature10990](https://doi.org/10.1038/nature10990)
- Gogichaishvili, D., Mamatsashvili, G., Horton, W., & Chagelishvili, G. 2018, *ApJ*, 866, 134, doi: [10.3847/1538-4357/aadbad](https://doi.org/10.3847/1538-4357/aadbad)
- Golightly, E. C. A., Coughlin, E. R., & Nixon, C. J. 2019, *ApJ*, 872, 163, doi: [10.3847/1538-4357/aafd2f](https://doi.org/10.3847/1538-4357/aafd2f)
- Gu, W.-M., & Lu, J.-F. 2007, *ApJ*, 660, 541, doi: [10.1086/512967](https://doi.org/10.1086/512967)
- Guillochon, J., & McCourt, M. 2017, *ApJL*, 834, L19, doi: [10.3847/2041-8213/834/2/L19](https://doi.org/10.3847/2041-8213/834/2/L19)
- Hawley, J. F., Gammie, C. F., & Balbus, S. A. 1995, *ApJ*, 440, 742, doi: [10.1086/175311](https://doi.org/10.1086/175311)
- Hayasaki, K., & Jonker, P. G. 2021, *ApJ*, 921, 20, doi: [10.3847/1538-4357/ac18c2](https://doi.org/10.3847/1538-4357/ac18c2)
- Hayasaki, K., Stone, N., & Loeb, A. 2013, *MNRAS*, 434, 909, doi: [10.1093/mnras/stt871](https://doi.org/10.1093/mnras/stt871)
- . 2016, *MNRAS*, 461, 3760, doi: [10.1093/mnras/stw1387](https://doi.org/10.1093/mnras/stw1387)
- Hayasaki, K., Zhong, S., Li, S., Berczik, P., & Spurzem, R. 2018, *ApJ*, 855, 129, doi: [10.3847/1538-4357/aab0a5](https://doi.org/10.3847/1538-4357/aab0a5)
- Hills, J. G. 1975, *Nature*, 254, 295, doi: [10.1038/254295a0](https://doi.org/10.1038/254295a0)
- Holoien, T. W. S., Prieto, J. L., Bersier, D., et al. 2014, *MNRAS*, 445, 3263, doi: [10.1093/mnras/stu1922](https://doi.org/10.1093/mnras/stu1922)
- Holoien, T. W. S., Kochanek, C. S., Prieto, J. L., et al. 2016, *MNRAS*, 463, 3813, doi: [10.1093/mnras/stw2272](https://doi.org/10.1093/mnras/stw2272)
- Holoien, T. W. S., Auchettl, K., Tucker, M. A., et al. 2020, *ApJ*, 898, 161, doi: [10.3847/1538-4357/ab9f3d](https://doi.org/10.3847/1538-4357/ab9f3d)
- Hung, T., Gezari, S., Blagorodnova, N., et al. 2017, *ApJ*, 842, 29, doi: [10.3847/1538-4357/aa7337](https://doi.org/10.3847/1538-4357/aa7337)
- Jafari, A., & Vishniac, E. T. 2018, *ApJ*, 854, 2, doi: [10.3847/1538-4357/aaa75b](https://doi.org/10.3847/1538-4357/aaa75b)
- Kajava, J. J. E., Giustini, M., Saxton, R. D., & Miniutti, G. 2020, *A&A*, 639, A100, doi: [10.1051/0004-6361/202038165](https://doi.org/10.1051/0004-6361/202038165)
- Kato, S., Fukue, J., & Mineshige, S. 2008, *Black-Hole Accretion Disks — Towards a New Paradigm —*. <https://ui.adsabs.harvard.edu/abs/2008bbhad.book.....K>
- Li, J., & Cao, X. 2019, *ApJ*, 872, 149, doi: [10.3847/1538-4357/ab0207](https://doi.org/10.3847/1538-4357/ab0207)
- Lightman, A. P., & Eardley, D. M. 1974, *ApJL*, 187, L1, doi: [10.1086/181377](https://doi.org/10.1086/181377)
- Liu, X.-L., Dou, L.-M., Chen, J.-H., & Shen, R.-F. 2022, *ApJ*, 925, 67, doi: [10.3847/1538-4357/ac33a9](https://doi.org/10.3847/1538-4357/ac33a9)
- Lodato, G., King, A. R., & Pringle, J. E. 2009, *MNRAS*, 392, 332, doi: [10.1111/j.1365-2966.2008.14049.x](https://doi.org/10.1111/j.1365-2966.2008.14049.x)
- Mageshwaran, T., Shaw, G., Bhattacharyya, S., & Hayasaki, K. 2023, arXiv e-prints, arXiv:2312.17417, doi: [10.48550/arXiv.2312.17417](https://doi.org/10.48550/arXiv.2312.17417)
- Matsumoto, R., & Tajima, T. 1995, *ApJ*, 445, 767, doi: [10.1086/175739](https://doi.org/10.1086/175739)
- Mummery, A., & Balbus, S. A. 2019, *MNRAS*, 489, 132, doi: [10.1093/mnras/stz2141](https://doi.org/10.1093/mnras/stz2141)
- Nicholl, M., Blanchard, P. K., Berger, E., et al. 2019, *MNRAS*, 488, 1878, doi: [10.1093/mnras/stz1837](https://doi.org/10.1093/mnras/stz1837)
- Nicholl, M., Wevers, T., Oates, S. R., et al. 2020, *MNRAS*, 499, 482, doi: [10.1093/mnras/staa2824](https://doi.org/10.1093/mnras/staa2824)
- Park, G., & Hayasaki, K. 2020, *ApJ*, 900, 3, doi: [10.3847/1538-4357/ab9ebb](https://doi.org/10.3847/1538-4357/ab9ebb)
- Pascucci, I., Cabrit, S., Edwards, S., et al. 2023, in *Astronomical Society of the Pacific Conference Series*, Vol. 534, *Protostars and Planets VII*, ed. S. Inutsuka, Y. Aikawa, T. Muto, K. Tomida, & M. Tamura, 567, doi: [10.48550/arXiv.2203.10068](https://doi.org/10.48550/arXiv.2203.10068)
- Petit, V., Wade, G. A., Drissen, L., Montmerle, T., & Alecian, E. 2008, *MNRAS*, 387, L23, doi: [10.1111/j.1745-3933.2008.00474.x](https://doi.org/10.1111/j.1745-3933.2008.00474.x)
- Piro, A. L., & Lu, W. 2020, *ApJ*, 894, 2, doi: [10.3847/1538-4357/ab83f6](https://doi.org/10.3847/1538-4357/ab83f6)
- Rees, M. J. 1988, *Nature*, 333, 523, doi: [10.1038/333523a0](https://doi.org/10.1038/333523a0)
- Roth, N., Rossi, E. M., Krolik, J., et al. 2020, *SSRv*, 216, 114, doi: [10.1007/s11214-020-00735-1](https://doi.org/10.1007/s11214-020-00735-1)
- Schmidt, G. D., Harris, H. C., Liebert, J., et al. 2003, *ApJ*, 595, 1101, doi: [10.1086/377476](https://doi.org/10.1086/377476)
- Shakura, N. I., & Sunyaev, R. A. 1973, *A&A*, 24, 337
- Starling, R. L. C., Siemiginowska, A., Uttley, P., & Soria, R. 2004, *MNRAS*, 347, 67, doi: [10.1111/j.1365-2966.2004.07167.x](https://doi.org/10.1111/j.1365-2966.2004.07167.x)

- Strubbe, L. E., & Quataert, E. 2009, MNRAS, 400, 2070,
doi: [10.1111/j.1365-2966.2009.15599.x](https://doi.org/10.1111/j.1365-2966.2009.15599.x)
- Suzuki, T. K., & Inutsuka, S.-i. 2009, ApJL, 691, L49,
doi: [10.1088/0004-637X/691/1/L49](https://doi.org/10.1088/0004-637X/691/1/L49)
- . 2014, ApJ, 784, 121, doi: [10.1088/0004-637X/784/2/121](https://doi.org/10.1088/0004-637X/784/2/121)
- Suzuki, T. K., Muto, T., & Inutsuka, S.-i. 2010, ApJ, 718,
1289, doi: [10.1088/0004-637X/718/2/1289](https://doi.org/10.1088/0004-637X/718/2/1289)
- Suzuki, T. K., Ogihara, M., Morbidelli, A., Crida, A., &
Guillot, T. 2016, A&A, 596, A74,
doi: [10.1051/0004-6361/201628955](https://doi.org/10.1051/0004-6361/201628955)
- Tchekhovskoy, A., Metzger, B. D., Giannios, D., & Kelley,
L. Z. 2014, MNRAS, 437, 2744,
doi: [10.1093/mnras/stt2085](https://doi.org/10.1093/mnras/stt2085)
- Velikhov, E. P. 1959, Zh. Eksp. Teor. Fiz., 36, 1398
- Wyrzykowski, L., Zieliński, M., Kostrzewa-Rutkowska, Z.,
et al. 2017, MNRAS, 465, L114,
doi: [10.1093/mnrasl/slw213](https://doi.org/10.1093/mnrasl/slw213)
- Xue, L., Sadowski, A., Abramowicz, M. A., & Lu, J.-F.
2011, ApJS, 195, 7, doi: [10.1088/0067-0049/195/1/7](https://doi.org/10.1088/0067-0049/195/1/7)
- Zhong, S., Hayasaki, K., Li, S., Berczik, P., & Spurzem, R.
2023, ApJ, 959, 19, doi: [10.3847/1538-4357/ad0122](https://doi.org/10.3847/1538-4357/ad0122)